

1 Multiple thermal AMOC thresholds in the intermediate complexity model Bern3D

2

3 Markus Adloff^{1,2*}, Frerk Pöppelmeier^{1,2}, Aurich Jeltsch-Thömmes^{1,2}, Thomas F. Stocker^{1,2},
4 Fortunat Joos^{1,2}

5

6 ¹ Centre for Environmental Physics, University of Bern, Switzerland

7 ² Oeschger Centre for Climate Change Research, University of Bern, Switzerland

8

9 *Contact: markus.adloff@unibe.ch

10

11 Abstract

12

13 Variations of the Atlantic Meridional Overturning Circulation (AMOC) are associated with
14 Northern Hemispheric and global climate shifts. Thermal thresholds of the AMOC have been
15 found in a hierarchy of numerical circulation models, and there is an increasing body of
16 evidence for the existence of highly sensitive AMOC modes where small perturbations can
17 cause disproportionately large circulation and hence climatic changes. We discovered such
18 thresholds in simulations with the intermediate complexity Earth system model Bern3D,
19 which is highly computationally efficient allowing for studying this non-linear behaviour
20 systematically over entire glacial cycles. By simulating the AMOC under different magnitudes
21 of orbitally-paced changes in radiative forcing over the last 788,000 years, we show that up
22 to three thermal thresholds are crossed during glacial cycles in Bern3D, and that thermal
23 forcing could have destabilised the AMOC repeatedly. We present the circulation and sea
24 ice patterns that characterise the stable circulation modes between which this model
25 oscillates during a glacial cycle, and assess how often and when thermal forcing could have
26 preconditioned the Bern3D AMOC for abrupt shifts over the last 788 kyr.

27

28 1 Introduction

29

30 The Atlantic Meridional Overturning Circulation (AMOC) transports warm waters from the
31 Southern Hemisphere and the Mexican Gulf towards the Nordic Seas, until the gradually
32 cooled salty water lost enough buoyancy and sinks, forming North Atlantic Deep Water
33 (NADW). This water mass moves southwards along the western boundary of the Atlantic
34 until it encounters the denser Antarctic Bottom Water (AABW) and slowly rises and upwells
35 in the Southern Ocean, being ultimately incorporated either into AABW or the lighter
36 Antarctic Intermediate Water (AAIW). The northward heat transport of the AMOC shapes
37 regional climate by pushing the polar front north by several degrees of latitude, effectively

38 producing a climate in Europe and Greenland that is milder than predicted from
39 latitude/insolation alone (Ruddiman and McIntyre 1981, Bard et al. 1987). It also affects
40 global climate by shifting the Intertropical Convergence Zone (ITCZ) and monsoon systems
41 (Wang et al., 2001, Bozbiyik et al., 2011), and interacting with the regional climate and deep
42 water formation in the North Pacific (Okazaki et al., 2010, Menviel et al., 2012, Praetorius
43 and Mix, 2014). The AMOC furthermore shapes biological surface productivity by regulating
44 nutrient supply to the surface ocean in the Atlantic and Pacific (Tetard et al., 2017, Joos et
45 al., 2017). On its southward path in the Atlantic, it influences deep ocean nutrient, carbon,
46 and oxygen concentrations (Broecker, 1991). By affecting primary production and deep
47 ocean carbon storage, AMOC changes also modulate atmospheric greenhouse gas
48 concentrations (e.g. Menviel et al., 2008). Rapid changes in AMOC and hence Atlantic heat
49 and carbon redistribution occurred repeatedly during the last glacial, termed Heinrich
50 (Heinrich, 1988, Broecker, 1994) and Dansgaard-Oeschger events (Oeschger et al., 1984,
51 Dansgaard et al., 1993), which had regional and global impacts on ecosystems and humans
52 (e.g. Severinghaus et al., 2009, Timmermann and Friedrich, 2016). Yet, the factors
53 determining AMOC stability are not fully understood.

54

55 As part of the thermohaline circulation, the AMOC is sensitive to both salinity and thermal
56 forcing. Depending on the location of deep water formation in both hemispheres, the AMOC
57 can switch between stable circulation states - either gradually or abruptly - as local vertical
58 density profiles, sea ice extent, and meridional heat and salinity gradients change. Numerical
59 experiments showed that large freshwater inputs into the North Atlantic can theoretically
60 cause abrupt shifts from a vigorous circulation state to a temporarily subdued or collapsed
61 circulation (e.g. Stocker and Wright, 1991, reviews by Weijer et al., 2019, Jackson et al.,
62 2023). Such possible shifts of circulation state were first identified in box models (Stommel
63 1961) and confirmed in intermediate complexity models and global circulation models
64 (Jackson and Wood, 2018, review in Jackson et al., 2023). ~~Systematic testing of AMOC
65 stability is done more easily in lower complexity models than General Circulation Models
66 (GCMs), but the existence of multiple AMOC equilibria seems to be determined by the
67 model-dependent existence and strength of feedbacks, with more complex models including
68 more, possibly counteracting, feedbacks (Weijer et al., 2019).~~ AMOC bistability could explain
69 reconstructed sudden AMOC state shifts in the Pleistocene, possibly caused by large
70 freshwater fluxes from melting continental ice shields and increased iceberg transport into
71 the North Atlantic at the onset of Heinrich Events (Broecker, 1994, Grousset et al., 2000).
72 Lags between the appearance of ice-rafted debris and the reconstructed cooling, however,
73 suggest that freshwater fluxes could have instead acted as a positive feedback to AMOC
74 weakening rather than triggering it (Barker et al., 2015).

75

76 Besides Heinrich event-like AMOC shifts to a less vigorous circulation in response to strong
77 freshwater forcing, there is increasing evidence for metastable AMOC states in-between the
78 glacial and interglacial circulation end-members. In some numerical models, and for narrow
79 parameter ranges (e.g. atmospheric CO₂ concentrations, ice sheet configurations), the
80 AMOC in such intermediate climate states is sensitive to small internal or external variability
81 ([e.g. Aeberhardt et al., 2000, Knutti et al., 2002, Zhang et al., 2014b, Zhang et al., 2017](#))
82 and can sustain spontaneous oscillations (~~e.g. Aeberhardt et al., 2000, Knutti et al., 2002,~~
83 ~~Zhang et al., 2014, Zhang et al., 2017~~; Brown and Galbraith, 2016, Vettoretti et al., 2022,
84 [Armstrong et al., 2022](#), review of CMIP6 models in Malmierca-Vallet et al., 2023). Some of
85 these oscillations could be analogues to Dansgaard-Oeschger events that have been
86 identified during intermediate glacial climate conditions, specifically during Marine Isotope
87 Stage (MIS) 3, and are thought to be caused by internal feedbacks that amplified small
88 changes of the North Atlantic salinity balance ([Zhang et al., 2014, Zhang et al., 2014b,](#)
89 [Zhang et al., 2017, Klockmann et al., 2020, Vettoretti et al., 2022, Armstrong et al., 2022](#)).
90 Meteoric and terrestrial freshwater input to the surface ocean are climate-dependent, as is
91 ice rafting and the salt rejection associated with sea ice formation. These processes are thus
92 impacted by, and impact themselves, the AMOC ([Ganopolski and Rahmstorf, 2001, Barker](#)
93 [et al., 2015](#)). Feedbacks similarly exist for the salinity transport from the tropics to the North
94 Atlantic, global circulation patterns, and the salinity gradients which determine salt transport
95 into the Atlantic basin through the Bering Strait, Drake Passage, and from the Indian Ocean
96 (e.g. Rahmstorf 1996). Besides salinity changes, numerical experiments with GCMs also
97 showed that the vertical temperature profile affects AMOC stability (Haskins et al., 2020).
98 Short-term AMOC weakening in response to warming has been simulated by a wide range
99 of GCMs (e.g. Mikolajewicz et al., 1990, Gregory et al., 2005, Weijer et al., 2020). Thermal
100 forcing of the North Atlantic has also been found to cause longer term gradual changes in
101 AMOC strength in intermediate and higher resolution models (Manabe and Stouffer, 1993,
102 Stocker and Schmittner, 1997, Knorr and Lohmann, 2007, Zhang et al., 2017, Galbraith and
103 Lavergne, 2019). In addition, bistability of AMOC under thermal forcing has been found in
104 uncoupled and coupled GCMs (Oka et al., 2012, Klockmann et al., 2018), and thermal
105 forcing, especially of the Southern Ocean, can cause abrupt AMOC state transitions similar
106 to hosing in the North Atlantic (Oka et al., 2021, Sherriff-Tadano et al., 2023). An important
107 process in the cooling-driven weakening of AMOC is the covering of former deep convection
108 sites with sea ice, which then causes a southward shift of deep convection (Oka et al.,
109 2012). Such a southward shift is only possible if the water column south of existing
110 convection sites is sufficiently destabilised by climate-driven density changes (Ganopolski
111 and Rahmstorf, 2001).

112

113 So far, simulations of thermal AMOC thresholds have mostly been conducted with
114 computationally expensive numerical models, ~~and the implications of the existence of AMOC~~
115 ~~instability and thermal thresholds have not been tested across entire glacial cycles. While~~
116 ~~providing crucial process understanding, the limited simulation length makes direct~~
117 ~~comparisons of these simulations to proxy timeseries challenging, which is required to~~
118 ~~assess the role of these processes in glacial-interglacial AMOC changes. The existence of~~
119 ~~multiple AMOC equilibria seems to be determined by the model-dependent existence and~~
120 ~~strength of feedbacks, with more complex models including more, possibly counteracting,~~
121 ~~feedbacks (Weijer et al., 2019). Yet, systematic testing of AMOC stability and long transient~~
122 ~~simulations are done more easily in lower complexity models than General Circulation~~
123 ~~Models (GCMs), and the implications of the existence of AMOC instability and thermal~~
124 ~~thresholds have not been tested across entire glacial cycles. While providing crucial process~~
125 ~~understanding, direct comparisons of these simulations to proxy records are therefore~~
126 ~~challenging.~~

127

128 Here, we demonstrate the existence of hysteresis and mode shifts in the AMOC in the
129 ~~computationally-efficient, intermediate complexity model Bern3D; under radiative forcing in~~
130 ~~the absence of freshwater hosing. Instead, we only apply changes in the radiative forcing to~~
131 ~~the atmosphere-ocean system. The model can be used to study AMOC changes with and~~
132 ~~without freshwater hosing over full glacial cycles.~~ We provide a comprehensive description of
133 the underlying processes ~~of the simulated AMOC response to radiative changes and~~
134 ~~elucidate their influence of radiative changes on the AMOC dynamics in the Bern3D model~~
135 ~~during orbitally-forced glacial-interglacial cycles in transient simulations of the last eight~~
136 ~~glacial cycles.~~

137

138 **2 Methods**

139

140 We employed the Bern3D intermediate complexity model version 2.0 (Müller et al., 2006,
141 Roth et al., 2014) to investigate the AMOC behaviour under a wide range of radiative forcing.
142 The Bern3D model comprises a 3D ocean component with a 40x41 horizontal grid and 32
143 depth layers, along with a 2D atmosphere (spatially-explicit energy-moisture balance with
144 prescribed wind fields) and dynamic sea-ice. The model explicitly calculates the thermo-
145 haline circulation with a frictional-geostrophic flow (Edwards et al., 1998) and contains
146 parameterizations to account for isopycnal diffusion and eddy-turbulence via the Gent-
147 McWilliams parameterization (Griffies, 1998). Temperature and salinity are dynamically
148 transported by the physical ocean model and respond to static seasonal wind fields and

149 changing atmospheric 2D energy and moisture balance, sea ice formation and external
 150 forcings. Bern3D explicitly calculates Pacific-Atlantic transport through the Bering Strait, and
 151 freshwater flux corrections are only imposed in the Weddell Sea, and compensated for in the
 152 Southern Ocean to induce stronger deep water formation (Ritz et al., 2011, Roth et al.,
 153 2014).

154

155 Table 1: Overview of the model experiments in this study. In set A, radiative forcing from
 156 dust is scaled linearly with $\delta^{18}\text{O}$ and assuming different magnitudes at LGM as given in
 157 parentheses.

158

Simulation Set	Simulation ID	Starting point and length	Forcing	Purpose
A	A0	MIS 19 spin-up 787500 years	orbital+GHG+dust(0 W/m ²)	test AMOC changes in response to transient glacial-interglacial radiative forcing
	A1		orbital+GHG+dust(-1 W/m ²)	
	A2		orbital+GHG+dust(-2 W/m ²)	
	A3		orbital+GHG+dust(-3 W/m ²)	
	A4		orbital+GHG+dust(-4 W/m ²)	
	A5		orbital+GHG+dust(-5 W/m ²)	
	A6		orbital+GHG+dust(-6 W/m ²)	
	A7		orbital+GHG+dust(-7 W/m ²)	
	A8		orbital+GHG+dust(-8 W/m ²)	
B	B.slow	PI spin-up, 105 kyr	linear change in RF from 0 to -10 W/m ² over 50 kyr and recovery over next 50 kyr	identify processes that cause AMOC shifts under radiative forcing
	B.slow.a	year 23000 of B.slow, 20 kyr	0.1 Sv freshwater input over 100 yr	test AMOC stability at different time steps in B.slow
	B.slow.b	year 24500 of B.slow, 20 kyr		
	B.slow.c	year 28500 of B.slow, 5 kyr		
	B.slow.d	year 47000 of B.slow, 5 kyr		
	B.fast.PI	PI spin-up, 25 kyr	linear change in RF from 0 to -10 W/m ² over 10 kyr and recovery over next 10 kyr with different orbital parameters	test dependence of AMOC response to radiative forcing to orbital constellation
	B.fast.21ka	PI spin-up, 25 kyr		
	B.fast.30ka	PI spin-up, 25 kyr		
	B.fast.50ka	PI spin-up, 25 kyr		
B.fast.80ka	PI spin-up with, 25 kyr			

159

160

161 We conducted two sets of simulations with the Bern3D model (Table 1). In set A, comprising
 162 nine simulations, we fully transiently simulated the last 788 kyr by imposing changes in
 163 orbital configuration, ice sheet albedo, and globally-averaged radiative forcing from the well-
 164 mixed greenhouse gases (GHG) CO₂ and CH₄ (combined here labelled as the ‘standard
 165 forcing’). The runs started from an interglacial steady state (50 kyr with pre-industrial (PI)
 166 conditions and 2 kyr of re-adjustment to the radiative balance of MIS 19c). Orbital (Berger,
 167 1978, Berger and Loutre, 1991), GHG (Bereiter et al., 2015, Loulergue et al., 2008, Joos and
 168 Spahni, 2008), and ice sheet albedo forcing (i.e. the standard forcing) is identical in each run
 169 (Fig. 1). Ice sheet albedo changes are calculated based on the benthic $\delta^{18}\text{O}$ LR04 stack

170 (Lisiecki & Raymo, 2005) smoothed by averaging over a 10000-year moving window for the
171 past 788 kyr.

172

173 The LR04 stack was chosen because it is the only complete record with constant temporal
174 resolution over the simulated period. In our experiments, we applied spatially-uniform
175 radiative forcings, to account for uncertainties in the glacial radiative balance, e.g. uncertain
176 atmospheric optical depth changes due to changes in aerosols and dust, in addition to the
177 better constrained temperature changes due to orbital changes and greenhouse gases,
178 hence termed dust forcing. The scale of this forcing varies between the simulations and
179 transiently within each simulation. The maximum radiative dust forcing, defined via the peak
180 LGM value in the smoothed $\delta^{18}\text{O}$ stack, is a free parameter, ranging from 0 to -8 W/m^2
181 relative to PI (Simulations A.0 to A.8). To construct the forcing, we scaled the maximum
182 forcing linearly with the smoothed LR04 stack, given the close correlation of reconstructed
183 dust fluxes and ice volume likely due to the dominant role of wind fields, sea level, and
184 hydrological cycle on dust fluxes (Winckler et al., 2008). The range of the resulting combined
185 radiative forcing is between -3 and -10 W/m^2 . This range brackets estimates of maximum
186 reductions in global mean radiative forcing at the LGM of $7 - 8 \text{ W/m}^2$ due to albedo,
187 greenhouse gas, and aerosol effects (Albani et al., 2018). The imposed forcings resulted in
188 global mean surface temperature (GMST) differences between the LGM and PI of -3 to -9.6
189 $^{\circ}\text{C}$. This temperature range encompasses most of the LGM-PI range reported in studies
190 investigating the Paleo Model Intercomparison Project (PMIP) 2, PMIP3, and PMIP4, which
191 range from -3.1 to $-7.2 \text{ }^{\circ}\text{C}$ (Masson-Delmotte et al., 2013, Kageyama et al., 2021).

192

193 Furthermore, these simulations are also consistent with proxy-based reconstructions that
194 indicate GMST differences between -2 and $-8 \text{ }^{\circ}\text{C}$ (Tierney et al., 2020), as well as covering
195 the $-6.1 \text{ }^{\circ}\text{C}$ GMST difference as constrained by a recent data assimilation study with the
196 CESM model (Tierney et al., 2020). It is important to note that we only considered the
197 radiative effect of an assumed uniform distribution of aerosols in our simulations. In reality,
198 this distribution would be non-uniform and aerosols would have additional effects on
199 atmospheric freshwater fluxes, two factors which are both relevant for AMOC stability
200 (Menary et al., 2013) but are poorly constrained for the last 788 kyr. Furthermore, freshwater
201 fluxes associated with the build-up and disintegration of continental ice sheets and glaciers
202 were not taken into account in any of the simulations presented here. We also kept the
203 topography constant and do not close the Bering Strait during glacial states.

204

205 Simulation set B (Tab. 1) was designed to investigate the mechanisms behind radiation-
206 driven AMOC changes under more idealised boundary conditions. This simulation set

207 | includes one long run with “slowly” changing radiative forcing [to a peak of \$-10 \text{ W/m}^2\$](#) (105 kyr,
208 B.slow), five short simulations with “fast” changing forcing (25 kyr, B.fast), and four
209 simulations branched off from B.slow at different points in time. B.slow started from a pre-
210 industrial state, followed by a linearly decreasing negative radiative forcing over 50 kyr,
211 followed by a linear increase of forcing back to the initial state also over 50 kyr (Figure 4).
212 We continued the simulation for an additional 5 kyr under constant, pre-industrial conditions
213 to let the model re-equilibrate. [The magnitude of this forcing is on the upper end of the range](#)
214 [explored in simulation set A \(A6-A8\).](#)

215 The setup of B.fast.PI is analogous to B.slow with the radiation decrease and consecutive
216 increase spanning 20 kyrs. The simulations started from a steady state with pre-industrial
217 orbital and GHG configuration, and were run with orbital configurations of PI, 21, 30, 50 and
218 80 kyrBP (simulations B.fast.PI, B.fast.21ka, B.fast.30ka, B.fast.50ka, B.fast.80ka,
219 respectively).

220

221 At four specific time points in B.slow, we branched off simulations to test the AMOC stability
222 by keeping all forcings constant, but at the same time applying a small freshwater hosing to
223 the North Atlantic (45°N - 70°N) with a magnitude of 0.1 Sv over 100 years. If the AMOC is in
224 a stable mode i.e. far from a bifurcation point, it should recover from these freshwater
225 perturbations returning to its initial strength, while an unstable AMOC close to a bifurcation
226 point should transition into a new circulation mode.

227

228 We incorporated three passive circulation tracers (‘dyes’) in set B. Each of these dye tracers
229 is restored to 1 at the surface of a chosen region (Fig. SI.1), and to zero elsewhere in the
230 surface ocean, and has no sources or sinks below the surface. In the deep ocean, the dye
231 tracer concentration is hence diluted only by mixing with other water masses sourced from
232 other regions. These artificial dye tracers allow us to track the dispersal of North Atlantic
233 Deep Water (NADW), Antarctic Intermediate Water (AAIW) and Antarctic Bottom Water
234 (AABW) in the ocean interior.

235

236

237 **3 Results and Discussion**

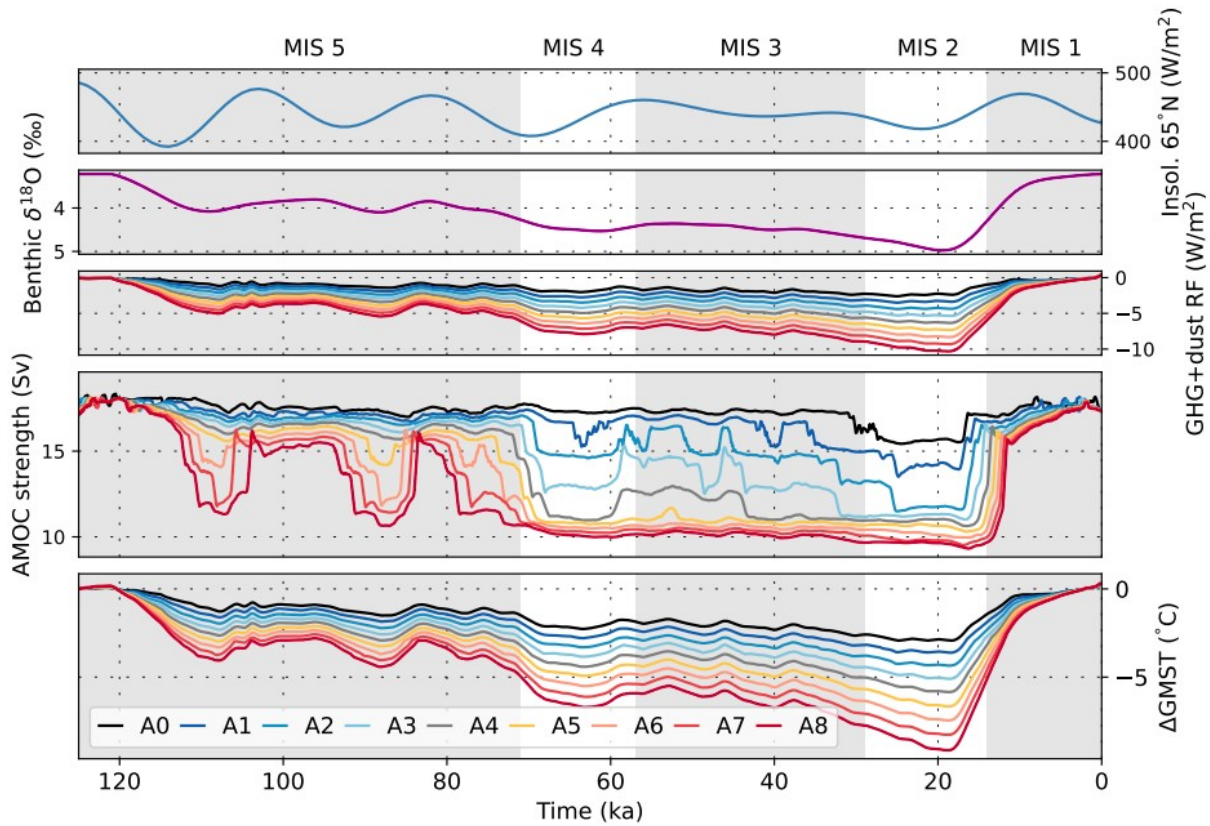
238

239 We first investigate the response of the AMOC to changes in orbital configuration and
240 radiative forcing as transiently simulated in our 788 kyr-long simulations of set A. We aim to
241 provide a comprehensive understanding of radiation-driven AMOC dynamics on glacial-
242 interglacial timescales. Subsequently, we utilise the more idealised setup of simulation set B
243 to further examine the underlying mechanisms driving these changes in more detail.

244

245

246 3.1. AMOC changes over the past eight glacial cycles



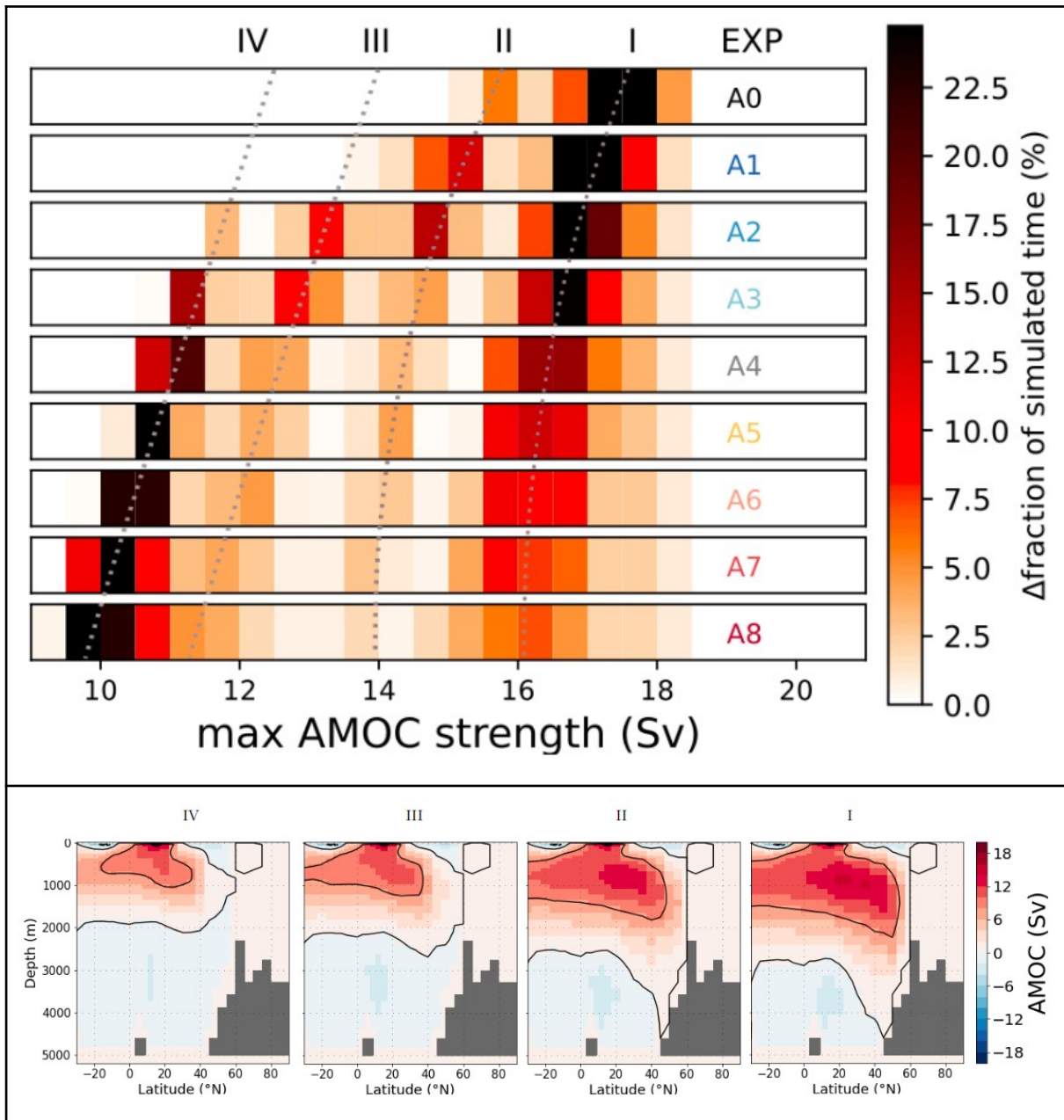
247

248 Figure 1: Forcings, AMOC and temperature response over the last 125 kyr of simulation
249 ensemble A. The upper three panels show July Insolation at 65°N, benthic $\delta^{18}\text{O}$ (10 kyr
250 spline of LR04, Lisiecki and Raymo, 2005) used to scale the dust forcing and the combined
251 effect of our dust forcing for each simulation and reconstructed atmospheric CO_2 changes
252 (Bereiter et al., 2015), smoothed with a second-order lowpass filter (cutoff frequency:
253 1/2000). The lower two panels show the 500 yr running mean of simulated AMOC strength
254 and GMST deviations from the PI in every simulation of simulation set A. Colours in the
255 lower two panels differentiate between simulations with different amplitudes of the
256 radiative forcing (see Methods).

257

258 In our simulations, radiative forcing- and orbitally-driven temperature changes resulted in
259 both gradual and abrupt AMOC shifts during each of the last eight glacial cycles (Fig. SI.2).
260 Fig. 1 illustrates the simulated AMOC threshold behaviour during these changes over the
261 entire last glacial cycle (past 125 kyr) with the different dust forcing scalings. Abrupt changes
262 in AMOC strength occurred in every simulation, with larger changes occurring under
263 stronger forcing. The magnitude of the dust forcing also determined the phase of the glacial
264 cycle during which the AMOC is most sensitive to radiative forcing: pronounced reductions in

265 radiative forcing under strong scaling resulted in a shift to the weakest AMOC mode early in
 266 the last glacial cycle, which is from then on insensitive to further changes induced by
 267 additional reductions in radiative forcing later on. Conversely, under weaker scaling, the
 268 initial decrease in forcing was insufficient to shift the AMOC out of its interglacial circulation
 269 mode.
 270
 271



272 Figure 2: Top: Fraction of each simulation in simulation set A (each over 788 kyr) during
 273 which a given maximum AMOC strength was simulated. Each row shows the results of one
 274 simulation, with the simulation ID on the right end of the column in colours that correspond to
 275 the lines in Fig 1. The bins are 0.5 Sv wide and four relative maxima in occurrence,

276 exhibiting distinct AMOC modes, I – IV, are indicated by dotted lines. Bottom: AMOC stream
277 function for the four circulation modes adopted across the last glacial cycle in simulation A3.

278

279 All simulations revealed multiple intermediate circulation modes between the glacial and
280 interglacial end-members. These modes manifested as distinct bands of increased
281 occurrence in Fig 2, which displays the fraction of the entire simulated period of 788 kyr
282 during which the AMOC exhibited a given maximum strength (binned into 0.5 Sv intervals).
283 The two intermediate modes II and III are distinguishable by AMOC strength, but not by their
284 meridional temperature or salinity gradients (Fig. SI.4), which questions whether these are
285 indeed separate circulation modes or expressions of one single mode that can have different
286 AMOC strengths (Lohmann et al. 2023). Yet, these circulation modes differ in global mean
287 and Greenland temperatures and North Atlantic Sea ice cover, suggesting that they are still
288 separate climate states (Fig. SI.5). Thus, we identified four frequently occurring circulation
289 modes in simulation set A that can be distinguished by AMOC strength, sea ice and
290 temperature, and three which can be distinguished by meridional temperature and salinity
291 gradients.

292

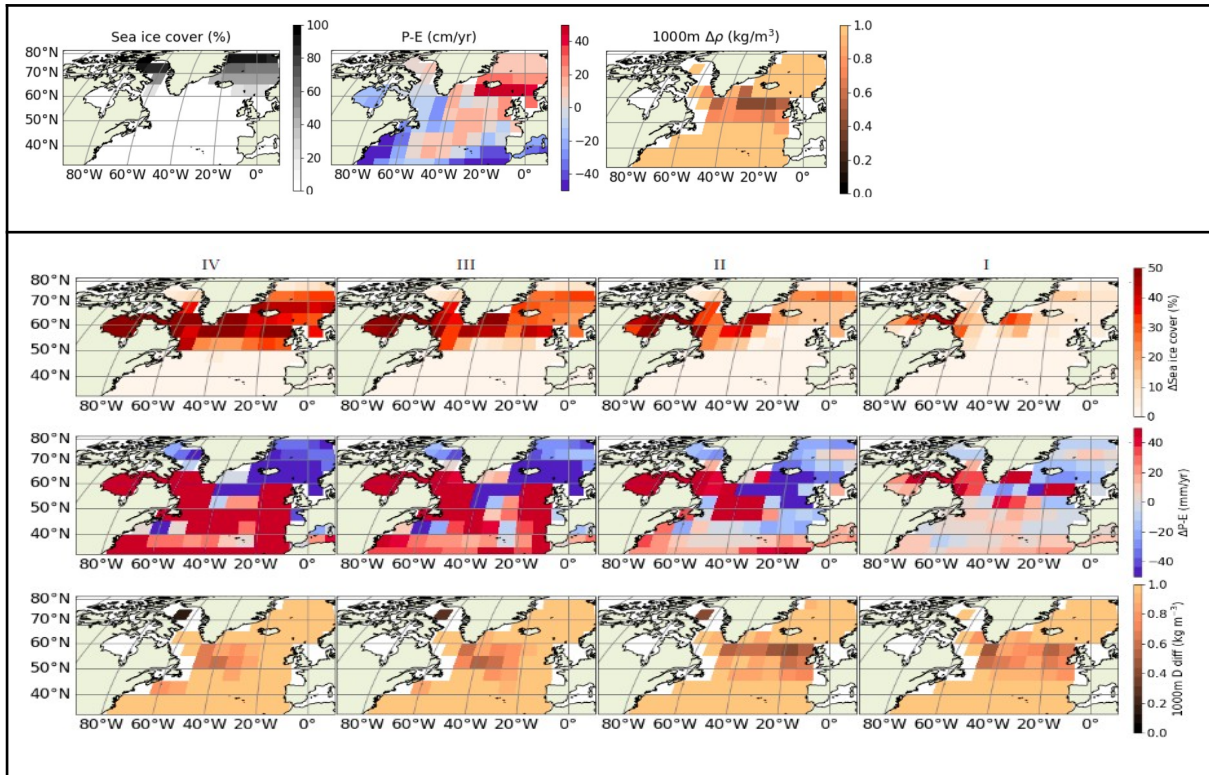
293 AMOC transitioned between these modes across the simulated glacial cycles due to
294 radiative forcing (Fig 2). The glacial and interglacial 'end-member' circulation modes I and IV
295 occurred most commonly: The AMOC was in either of these two modes for 62-85% of the
296 simulated 788 kyr, depending on the dust forcing scaling. The AMOC was found in the
297 intermediate circulation modes II and III most commonly under weak dust forcing. For
298 stronger forcings, AMOC transitioned quickly through these modes, which were therefore
299 less frequently occupied. Thus, it appears that there is a tendency towards bi-modal AMOC
300 stability under strong forcing scaling, where the AMOC was almost exclusively either in the
301 glacial or interglacial circulation mode. Once AMOC had adopted the weakest mode,
302 additional reductions in radiative forcing only caused minor additional and gradual AMOC
303 weakening and did not cause another abrupt transition.

304

305 The simulations A3 and A4 with intermediate glacial-interglacial temperature changes (LGM-
306 PI Δ GMST -5 to -6 °C, similar to the -6.1 °C constrained by Tierney et al., 2020)
307 predominantly exhibited AMOC transitions between the interglacial (mode I, ~16-17 Sv) and
308 glacial mode (mode IV, ~11 Sv), with two rarer intermediate circulation modes in-between.

309

310



311 Figure 3: Top row: Initial annually averaged sea ice cover, meteoric freshwater balance, and
 312 the density difference over the uppermost 1000 m of the water column in the North Atlantic
 313 (upper panel). Panels below: Changes of Differences relative to the initial state for the
 314 annually averaged sea ice cover, meteoric freshwater balance, and the density difference
 315 over the uppermost 1000 m of the water column in the four circulation modes. over the first
 316 30 kyr of simulation B. slow in the lower panel.

317

318 The interglacial circulation mode (mode I in Figs. 2 and 3) is characterised by NADW
 319 formation in the subpolar North Atlantic, specifically south of Greenland and close to the
 320 British Isles, as indicated by the small density difference over the upper 1000 m of the water
 321 column. In the first intermediate AMOC mode (II), deep water formation is enhanced in the
 322 Eastern Atlantic while it weakens in the West as sea ice expands further South (Fig. 3). The
 323 next intermediate circulation mode (III) is marked by a reduction in deep water formation in
 324 the eastern North Atlantic, as the local water column increasingly stratifies. Deep water
 325 formation continues south of the sea ice edge in the western North Atlantic, albeit
 326 substantially weakened. As the northwards transport of subtropical water diminished under
 327 further cooling, the AMOC transitioned into the glacial stable mode (IV). In this mode,
 328 convection in the North Atlantic is strongly reduced and cold, fresh surface waters stratify the
 329 water column off the European coast. At this point, additional negative radiative forcing
 330 enhanced the amplitude of the temperature and salinity anomalies but without triggering
 331 additional changes in the North Atlantic circulation pattern.

332

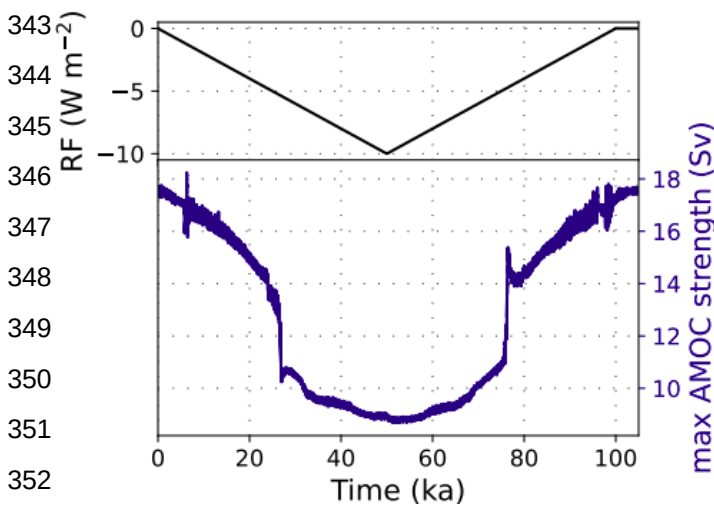
333 Our simulations cover four glacial cycles before the Mid-Brunhes transition (MBT, MIS 12
334 and MIS 11 (~430 ka)) and four thereafter. This transition was marked by a shift to warmer
335 interglacials with higher atmospheric CO₂ concentrations. There are only small differences
336 between the distributions of AMOC modes before and after the transition (fig SI.2), and none
337 are statistically significant in the two-sided Smirnov test, which determines the likelihood that
338 two distributions are the same (Berger and Zhou, 2014), even at the 50% confidence level.

339

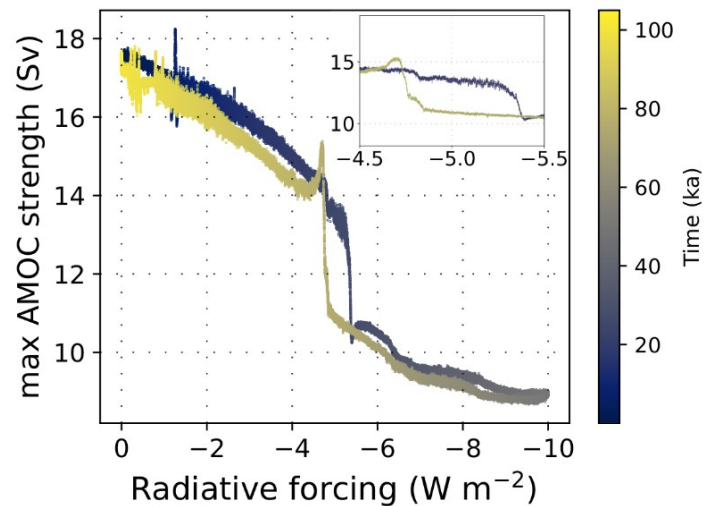
340 3.2. Processes responsible for the AMOC changes

341

342 a)



342 b)



354 Figure 4: Simulation B.slow: (a) Response of the AMOC to changes in radiative forcing
355 relative to the pre-industrial. The radiative forcing was linearly decreased over 50 kyr to a
356 minimum of $-10 W/m^2$ and then increased again at the same rate. (b) The associated
357 hysteresis loop of the AMOC under the radiative forcing, with the inset providing an enlarged
358 view of the hysteresis loop.

359

360

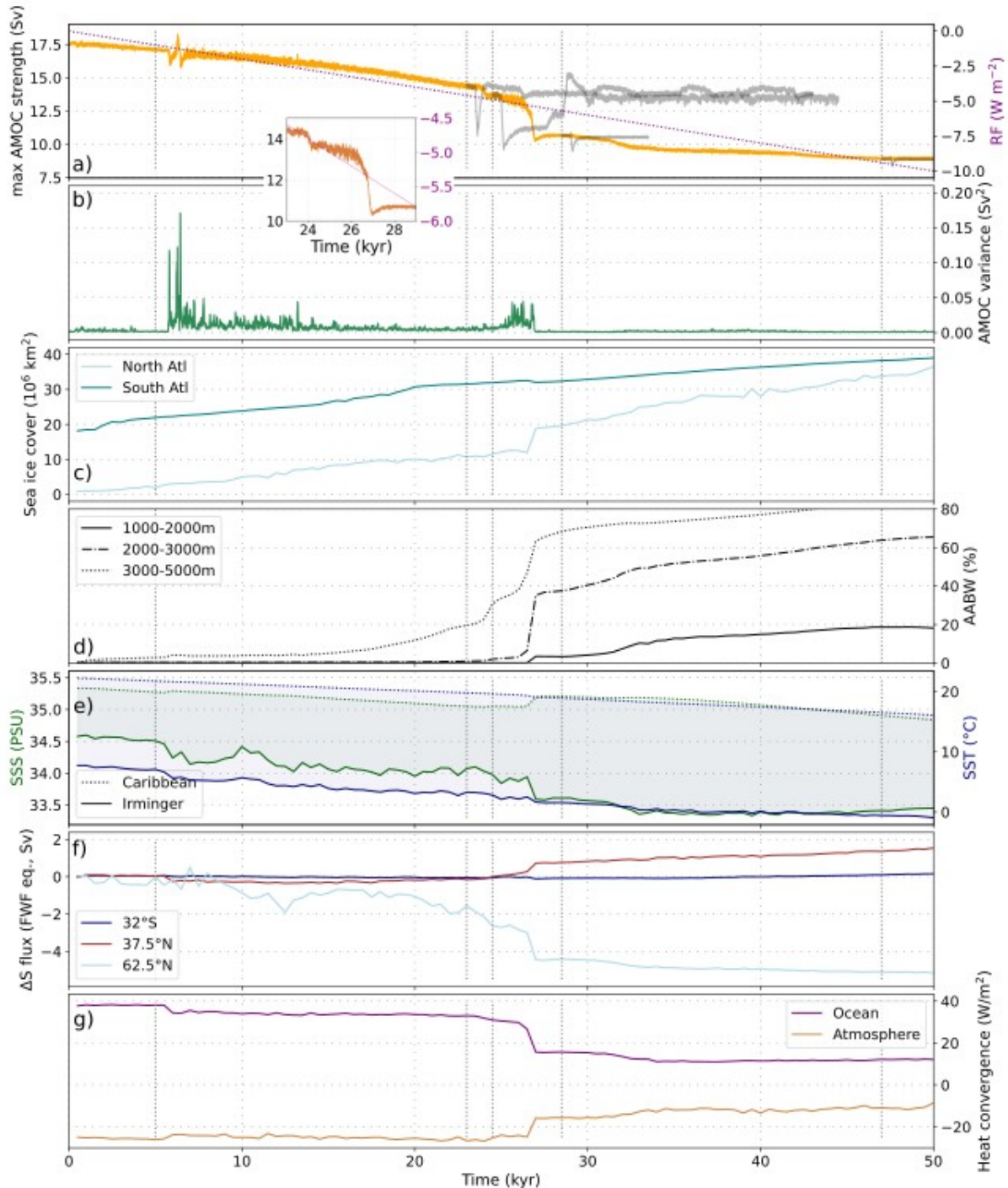
361

362

363

364

365



366
 367 Figure 5: Changes in ocean properties during the cooling phase in simulation B.slow. a)
 368 AMOC strength and the applied radiative forcing. At four points in time throughout B.slow,
 369 simulations were branched off to test the stability of the respective circulation mode (shown
 370 in dark grey). In these simulations, we kept the radiative forcing constant but applied a small
 371 freshwater perturbation after 500 yrs, before allowing the model to re-equilibrate (see
 372 Methods). b) AMOC variance calculated in a 50 yr moving window. c) Sea ice cover in the
 373 North Atlantic between 50-60°N ('North Atl', light blue) and the Atlantic sector of the
 374 Southern Ocean 50-68°S ('South Atl', teal). d) Volume fraction of AABW at three different

375 depth intervals in the subpolar North Atlantic (50-60°N). e) SST and SSS in the Caribbean
376 and Irminger seas. f) Change in the northward salinity transport by ocean currents in
377 freshwater flux (FWF) equivalents at different latitudes (following Liu et al., 2017). g)
378 Column-integrated heat flux convergence due to ocean circulation and heat loss to the
379 atmosphere (negative = heat loss by ocean) for the North Atlantic (40°N-70°N). Dotted
380 vertical grey lines indicate time points in the simulation at which we branched off stability
381 tests, and at which we analysed water mass distributions in Fig. 6.

382

383 In our simulations, the primary processes controlling the AMOC strength under changing
384 radiative forcing are density changes due to heat and salinity redistributions. We investigated
385 these in more detail in experiment B.slow (Fig. 4 and 5). This experiment is characterised by
386 a slow linear decrease in radiative forcing over 50 kyr, before it is increased again to the pre-
387 industrial value with the same rate of change (Fig. 4). Fig. 5 shows that AMOC weakened
388 gradually over the first 24 kyr, then weakened abruptly by 1 Sv at 24 kyr into the simulation
389 and by ~3 Sv at 27 kyr, and then continued to weaken gradually until the forcing is reversed
390 (Fig. 5a). In addition to the abrupt transition in AMOC strength, we found several additional
391 rapid changes in AMOC variability, heat, and salt fluxes (Fig. 5) and regional density profiles
392 (Fig. SI.7-9) which were not associated with persistent changes in AMOC strength, e.g. at 6
393 kyr into the simulation. In fact, experiment B.slow shows that a cascade of changes with little
394 effect on the mean AMOC strength occurred before the first abrupt AMOC weakening after
395 24 kyr. Since these changes might partially be artifacts of our coarse model resolution, we
396 here only focus on the larger scale changes instead. Initially, the whole Atlantic surface
397 ocean cooled and freshened, leaving the temperature and salinity differences between the
398 Irminger and Caribbean Seas almost unchanged (Fig 5e). However, NADW became less
399 salty and colder as a consequence of the changes in the surface ocean (not shown) and the
400 vertical density profiles in the subpolar North Atlantic steepened due to the surface
401 freshening and deep ocean cooling temperature and salinity changes (Fig. SI.7-8).

402

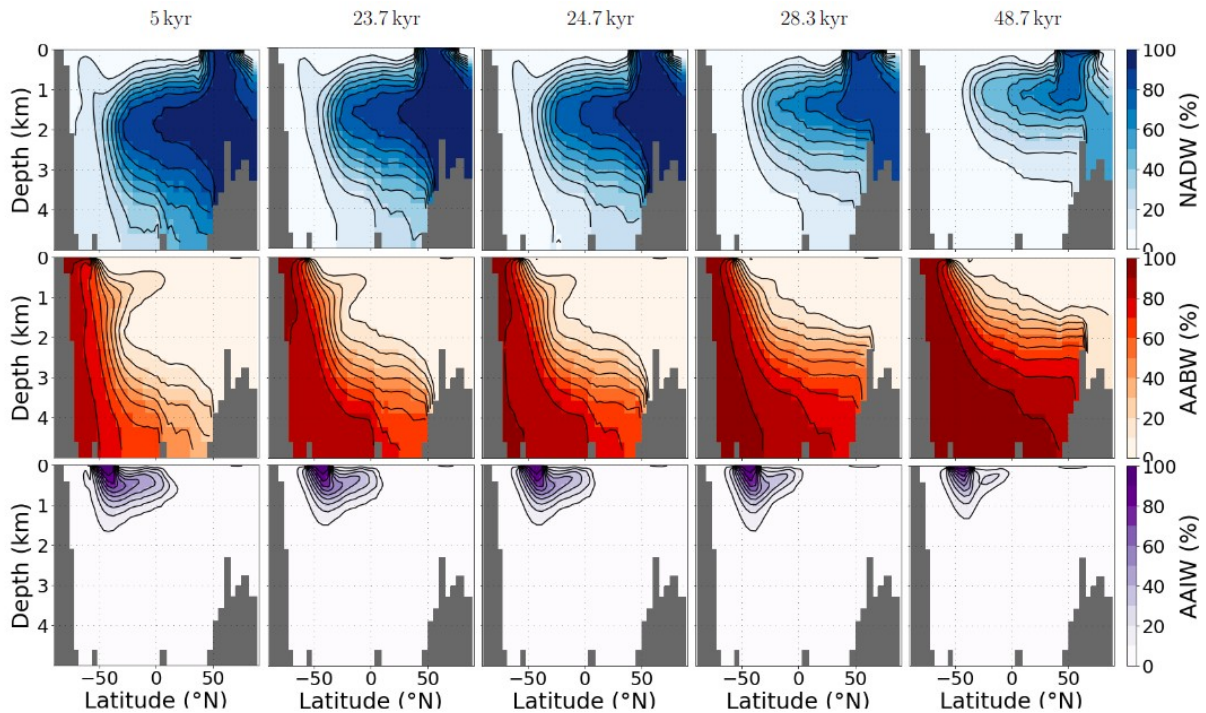
403 After about 6 kyr, ~~the changes in the North Atlantic density profile shifted the location of~~
404 ~~NADW formation:~~ NADW formation moved south as surface freshening stabilised vertical
405 density profiles in the subpolar east North Atlantic ~~stabilised under a freshening of the~~
406 surface and density profiles further south steepened due to surface cooling combined with
407 subsurface warming (Fig. SI.7-9). These changes did not cause a step-change in AMOC
408 strength, but freshwater and heat advection into the North Atlantic was reduced (Fig. 5f, g),
409 which reduced North Atlantic SST and SSS (Fig. 5e). ~~s~~Sea ice expansion increased in the
410 eastern North Atlantic, and AMOC variance (calculated over a moving 50-year window) was
411 increased (Fig. 5). ~~Transport of heat and salinity into the North Atlantic decreased (Fig. 5f,~~

412 | ~~g), which reduced North Atlantic SST and SSS (Fig. 5e).~~ The reduced influx of subtropical
413 surface waters also caused abrupt cooling and freshening in the Irminger Sea (Fig. SI.8). At
414 24 kyr, the AMOC had weakened to ~14.5 Sv and sea ice cover extended south of the
415 Irminger Sea (Fig SI.11). At this point, the AMOC strength dropped abruptly by 1 Sv, and
416 then by an additional 3 Sv ~3 kyr later, as the reduced salinity advection into the North
417 Atlantic and ~~precipitation and evaporation changes~~ a net increase in precipitation minus
418 evaporation (P-E) led to a strong surface freshening. As a result of the North Atlantic density
419 changes, the main North Atlantic convection site shifted southwards (determined by changes
420 in the vertical density profiles, Fig SI.10). Sea ice also increasingly covered former areas of
421 deep water formation in the North Atlantic. In the weakest circulation mode, the location of
422 the maximum AMOC stream function shifted southwards by approximately 10 degrees and
423 up in the water column by 400 m initially (28.5 kyr) and eventually almost 800 m (47 kyr)
424 This shift allowed cold, less dense water masses to extend further south into the North
425 Atlantic.

426

427 In the Southern Ocean, the cooling enhanced Southern Ocean deep water formation early
428 on in the experiment and led to a continuous expansion of sea ice in the Southern
429 Hemisphere. The biggest AMOC weakening at ~27 kyr was also accompanied by a very
430 weak bipolar seesaw effect (Stocker and Johnsen, 2003), which caused a temporary decline
431 in sea ice coverage in the Atlantic sector of the Southern Ocean (Fig. 5). ~~#This sea ice~~
432 decline was, however, was too small to reduce the radiation-driven sea ice increase in the
433 longer term. Both shifts in AMOC strength were accompanied by an increased spread of
434 AABW into the North Atlantic (Fig. 5d). The volume of AABW in the deep Atlantic influences
435 AMOC stability (Zhang et al., 2013, Galbraith and Lavergne, 2019). Thus, the spread of
436 AABW into the deep North Atlantic after the first AMOC shift at ~24 kyr might have
437 preconditioned the AMOC for the following shift at ~27 kyr in B.slow.

438



439
 440 Figure 6: Atlantic water mass distributions at the five time slices of our simulation B.slow
 441 indicated in Fig. 5. Each row shows the zonally-averaged contribution of water sourced in
 442 one of three regions: the North Atlantic (upper row), the Southern Ocean (middle row), and
 443 the Southern Atlantic (bottom row), diagnosed with three passive dye tracers. Fig. SI.1
 444 shows the spatial pattern of our dye forcing.

445
 446 The changes in the AMOC stream function associated with the decreasing radiative forcing
 447 in experiment B.slow bear close resemblance to the changes we observed in the transient
 448 experiment set A during AMOC transitions from the interglacial to the glacial circulation
 449 mode (Fig. 6 and Fig. SI.12 - SI.14).

450
 451 We tracked the effects of these circulation changes on the Atlantic distribution of
 452 intermediate and deep water masses as diagnosed from artificial dye tracers (see Fig SI.1
 453 for their source regions). Figure 6 shows that, during the first 23 kyr of our simulation, AABW
 454 slowly spread further North and occupied increasingly shallower depths while the northward
 455 reach of AAIW was reduced. Accordingly, NADW shoaled as it was unable to sink further
 456 when encountering AABW in the deep North Atlantic. The reduced export of NADW also led
 457 to a decrease in its southward extent, contracting to 40°S. The first abrupt shift in AMOC
 458 strength occurred at 24.5 kyr in B.slow and had only small effects on the water mass
 459 distribution. It mainly led to a reduced fraction of NADW at intermediate depths of the North
 460 Atlantic >45°N and a small increase of AABW in the abyssal North Atlantic (Fig. 5d). The
 461 following AMOC shift at 27 kyr reduced AMOC strength by more than 3 Sv, and was hence

462 also more strongly expressed in changes in the water mass distribution. It was accompanied
463 by a further reduction of NADW export into the deep Atlantic, before NADW was entirely
464 replaced by AABW at depths below ~ 3.5 km in the weakest circulation mode. AAIW was
465 increasingly curtailed in its northward reach, until it effectively no longer extended toward the
466 equator ($<10\%$).

467

468 In summary, in our simulation deep convection diminished first in the Irminger Sea while
469 deep water formation continued in the subpolar Northeast Atlantic and south of Greenland.
470 As sea ice extended into the Eastern North Atlantic south of Greenland and vertical density
471 profiles steepened further south, the northward reach of the AMOC was restricted and a new
472 circulation mode was established with increased sea ice cover $>55^\circ\text{N}$. The weakened
473 northwestward transport of heat and salt due to the reduced AMOC strength led to a
474 relatively fresh and cold eastern North Atlantic, stabilising the water column in the region and
475 producing another persistent AMOC mode. The simulated step changes in AMOC strength
476 in our simulations were thus the response to gradual surface cooling and freshening, and
477 occurred when NADW formation shifted southwards. The resulting redistributions of heat
478 and salinity caused sudden shifts in the vertical density profiles and sea ice expansion which
479 consolidated the new circulation mode (Ando and Oka, 2021). In particular, reduced
480 advection of heat and salinity into former locations of deep water formation resulted in a
481 more stable local water column (Fig. SI.7-9). The deep water formation regions are sensitive
482 to heat and salt flux changes, because any reduction in sea surface temperatures (SST)
483 increases surface density but simultaneously reduces evaporation in ice-free areas, thus
484 effectively creating a small freshwater forcing and a negative feedback to the buoyancy
485 changes caused by the initial SST decrease. Sea ice covering the downwelling areas
486 stabilises the water column by preventing surface ocean cooling and evaporation. The
487 progressive influx of AABW into the North Atlantic is a further process stabilising new
488 circulation modes by stratifying the water column from below (Buizert and Schmittner, 2015).
489 The difference between freshwater transport into the South Atlantic at 32°S and into the
490 Arctic at 62.5°N in Fig. 5f can be used as a measure for the basin-wide salinity feedback
491 (Rahmstorf, 1996, de Vries and Weber, 2005). In our simulation, changes in this metric were
492 predominantly caused by changes in the transport across the northern edge, since transport
493 into the South Atlantic remained almost unchanged throughout the cooling phase of B.slow.
494 North Atlantic salinity is instead governed by changing transport from the subtropics into the
495 North Atlantic and between the North Atlantic and Arctic. As such, [in our simulations it](#)
496 [seems](#) the processes involved in the sudden AMOC strength changes, namely density
497 changes in the upper water column, and those that stabilised new circulation modes (salinity
498 and heat redistributions, sea ice expansion) mostly operated in the North Atlantic region.

499

500 Our stability experiments demonstrated that the circulation modes before and after the
501 abrupt shifts recovered from small freshwater perturbations, and can thus be considered
502 stable, i.e. sufficiently far from bifurcation points to recover from the small perturbation (Fig.
503 5a, Fig. SI.6). In these branched off sensitivity tests, the circulation mode adopted before the
504 first AMOC threshold (at ~24 kyr), showed increased variability in the order of 0.5 Sv. The
505 next circulation mode (~25 kyr) responded most strongly to small freshwater perturbations
506 and was also the only circulation mode in our simulation which showed gradually increasing
507 AMOC variability (as determined by an increase in its variance) while approaching the next
508 threshold (Fig. 5a, Fig. SI.6). When the forcing was reversed, the radiation increase
509 gradually strengthened the AMOC until it rapidly transitioned back into the stronger
510 circulation mode when North Atlantic sea ice had receded sufficiently for a northward shift of
511 the convection sites and evaporation and salinity transport resumed. The radiative forcing at
512 which the AMOC transitioned from one circulation mode to the other was not equal for
513 decreasing and increasing radiative forcing: a stronger negative radiative forcing was
514 required to push the AMOC into its weak circulation mode than for the transition out of it (Fig.
515 4b).

516

517 Our sensitivity tests with different orbital configurations indicated that the existence of AMOC
518 thresholds under radiative forcing was not dependent on the initial orbital configuration.
519 However, the AMOC was slightly more sensitive to perturbations when initiated with the
520 orbital configuration equivalent to 30 ka before present. In this case, the threshold for the
521 AMOC to transition to its weaker mode was reached ~1 kyr earlier than under PI or 50 ka
522 orbital configurations (simulations B.short.30ka, B.short.PI, Fig. SI.15). The processes that
523 affected AMOC behaviour in simulation set B also caused AMOC changes over the
524 transiently simulated 788 kyr in simulation set A, but the circulation modes adopted varied
525 slightly in sea ice extent, hydrological cycle and salinity distribution under varying orbital
526 configurations.

527

528

529 **3.3. Comparison with other modelling studies and proxy data**

530

531 In our transient simulations covering the past 788 kyr, the AMOC strength decreased during
532 glacial phases solely due to changes in the hydrological cycle and sea ice that were induced
533 by orbital, greenhouse gas, and the additional radiative cooling. The existence of multiple
534 stable AMOC modes under varying thermal or radiative forcings has been found in various
535 GCMs (e.g. Knorr and Lohmann, 2007, Oka et al., 2012, Banderas et al., 2012, Brown and

536 Galbraith, 2016, Zhang et al., 2017, Klockmann et al., 2018). In agreement with previous
537 studies, we found multiple persistent AMOC circulation modes with distinct AMOC strengths
538 for radiative forcing levels between full glacial and interglacial climate states. Moreover, we
539 found that the transitions between these modes occur abruptly, some within as little as 100
540 years. In accordance with Lohmann et al. (2023), we found that these shifts in AMOC
541 strengths are preceded by cascades of density and circulation field changes, the number
542 and sequence of which depend on the strength of the forcing. Similar to the findings from
543 Oka et al. (2021), AMOC transitions arise primarily from salt redistribution in the ocean and
544 sea ice expansion into deep convection zones.

545

546 | In our simulations [A and B](#), each transition in AMOC strength was associated with a shift in
547 the convergence of heat and salt fluxes and a southward expansion of sea ice into the North
548 Atlantic. Sea ice cover decouples the surface ocean buoyancy from the atmosphere. In the
549 intermediate modes, locations with steep density gradients are close to a critical annually-
550 averaged sea ice cover. In these modes, small changes in sea ice cover can cause large
551 changes in surface buoyancy and the extent and location of deep convection, which makes
552 the AMOC sensitive to small perturbations. The AMOC was only pushed into its weakest
553 mode when all former convection sites in the subpolar North Atlantic were sea ice-covered
554 and heat convergence in the North Atlantic was strongly reduced.

555

556 | In their examination of thermal forcing of both hemispheres [in COCO, the ocean component](#)
557 [of MIROC](#), Oka et al. (2021) found that thermal AMOC thresholds only exist ~~in COCO, the~~
558 ~~ocean component of MIROC~~, if the Southern Hemisphere is cooled more than the Northern
559 Hemisphere. In contrast, Zhang et al. (2017) found sudden AMOC changes due to
560 greenhouse gas changes without a special focus on the Southern Hemisphere. In our
561 simulations with Bern3D, we also found thermal thresholds with similar cooling rates in both
562 hemispheres, but only after salinity re-distributions and changing meteoric freshwater fluxes
563 in response to about six thousand years of global cooling. [Thus, in our model, Southern](#)
564 [Hemisphere cooling does not need to exceed the cooling of the Northern Hemisphere to](#)
565 [affect AMOC but further sensitivity tests would be required to establish the relevance of](#)
566 [cooling in each hemisphere separately \(as shown in Oka et al., 2021\).](#)

567

568 | It is possible that changing meteoric freshwater fluxes are essential for the existence of such
569 a thermal threshold, which does not therefore appear in ~~an ocean model COCO~~ without a
570 thermally responsive atmosphere with a climate-driven freshwater balance. In a model with a
571 dynamic energy moisture balance component, atmospheric cooling reduces evaporation and
572 the water-holding capacity of the atmosphere. With this feedback enabled [in our model](#),

573 cooling can then affect seawater density directly via changing temperatures, and indirectly
574 via changing the meteoric freshwater balance and surface salinities. These changes would
575 induce additional kinematic changes (i.e., in the wind fields) in fully dynamic atmosphere
576 models but are kept constant in our simulations, i.e. in our simulations the moisture content
577 of air changes with climate but not the direction or strength of winds which disperse it. ~~In our~~
578 ~~model, a~~ decrease in the water-holding capacity of air therefore directly leads to a
579 reduction of the large-scale atmospheric moisture transport from low to high latitudes.

580 ~~Accordingly, wind stress fields are also kept constant here. Changes in wind stress have~~
581 ~~been documented to exert important controls on AMOC stability (e.g. Arzel et al., 2008;~~
582 ~~Yang et al., 2016) and thermal thresholds (Oka et al., 2012). These effects have been~~
583 ~~investigated in detail with the Bern3D model by Pöppelmeier et al. (2021) focusing on LGM~~
584 ~~boundary conditions.~~

585

586 The primary importance of salinity and heat redistributions as well as sea ice extent in the
587 North Atlantic for the simulated AMOC shifts resembles the findings from Ando and Oka
588 (2021)'s hosing experiments under LGM conditions and Zhang et al. (2017)'s simulations of
589 AMOC shifts in response to CO₂ changes under intermediate-glacial conditions. While our
590 experiments were run with pre-industrial topography, sea level and wind fields, the initial
591 location of convection sites between Greenland and the British Isles (areas with lowest
592 density differences over upper 1000 m in Fig. SI.11) resembles the LGM and intermediate-
593 glacial circulation modes in Ando and Oka (2021) and Zhang et al. (2017).

594

595 Ganopolski and Rahmstorf (2001) found that the possibility of a southward shift of deep
596 convection depends on the latitude of prior deep convection and the density field further
597 south, and Oka et al. (2012) showed that the location of deep convection and its distance
598 from the winter sea ice edge define thermal thresholds in AMOC strength. Several controls
599 on the location and strength of deep convection in the North Atlantic, that would have
600 affected AMOC stability over glacial cycles, have been established. Changes in wind stress,
601 for example, have been documented to exert important controls on AMOC stability (e.g.
602 Arzel et al., 2008, Yang et al., 2016) and thermal thresholds (Oka et al., 2012), but in our
603 simulations wind stress is constant. ~~Besides wind fields,~~ the location of deep convection is
604 further dependent on ~~wind fields,~~ climate and sea level/bathymetry (Ganopolski and
605 Rahmstorf, 2001, Oka et al., 2012, Zhang et al., 2014b, Zhang et al., 2017), and thus the
606 thermal AMOC thresholds are model and forcing dependent (Oka et al., 2012). Our
607 simulations capture the albedo effect of varying terrestrial ice sheet extent, but we did not
608 consider their orography or sea level effects, including impacts on the atmospheric
609 circulation, which were shown to affect AMOC (Li and Born, 2019; Pöppelmeier et al., 2021).

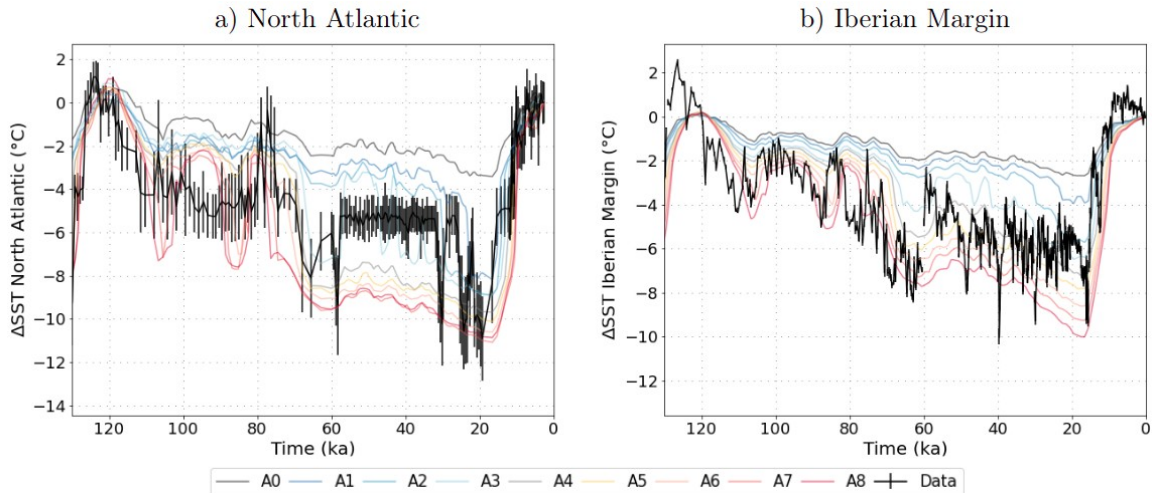
610 Previous studies suggested that pre-industrial or intermediate glacial ice sheet
611 configurations are required to even produce a thermal AMOC threshold in the range of
612 glacial-interglacial CO₂ concentrations in a full GCM and that the presence of a full glacial
613 Laurentide ice sheet prevents such a threshold (e.g. Klockmann et al., 2018). Northern
614 Hemisphere ice sheets also affect the composition and volume of AABW through
615 teleconnections (Galbraith and Lavergne, 2019), and the buoyancy difference between
616 AABW and NADW, as well as their fraction in Atlantic deep water, have been found to
617 precondition AMOC stability (Zhang et al., 2013). In addition, changes in the interconnection
618 of marine basins, specifically the Bering Strait, also affect AMOC stability (Hu et al. 2012).
619 The values of the thermal thresholds in our experiments are thus likely sensitive to the model
620 design and initiation. Pöppelmeier et al. (2021) showed that the sensitivity of Bern3D to
621 freshwater hosing increases when additional LGM boundary conditions are prescribed
622 (changed wind fields, closed Bering Strait, tidal mixing differences due to sea level changes).
623 The different wind fields and tidal mixing strengthened AMOC and increased the salt and
624 heat transport into the subpolar North Atlantic. This could mean that stronger cooling is
625 required to stabilise the water column in the Irminger Sea and reach the first thermal
626 threshold, when the full range of glacial boundary conditions are applied. Closure of the
627 Bering Strait increased the salt advection feedback, which stabilises the weak circulation
628 state without deep water formation in the subpolar North Atlantic.

629

630 Further investigations are needed to determine how changes in strength and location of the
631 wind stress due to the ice sheet's orography, sea level and Bering Strait closure would affect
632 sea ice formation in the northern North Atlantic and the AMOC thresholds in our simulations
633 quantitatively. Since we chose to focus only on radiation driven AMOC changes in our
634 experiments, while in reality AMOC was also influenced by freshwater flux changes,
635 particularly during Heinrich events, we would not expect a close model-data match with
636 reconstructed millennial-scale AMOC changes in the from- paleo-records. Still, we can
637 compare the long-term evolution of AMOC strength in our simulations and the
638 reconstructions. Our simulations show that the reconstructed glacial-interglacial temperature
639 changes had the potential to alter the density field in the North Atlantic by redistributing heat
640 and salt, and that some of these changes might have resulted in abrupt changes of AMOC
641 strength. By testing a wide range of glacial-interglacial temperature changes, our
642 experiments demonstrate that the cooling during glacial periods likely contributed to a
643 weakened AMOC. The strength and timing of the weakening depends on the actual
644 temperature change in the North Atlantic which would have been modulated by changes in
645 winds and ice shields.

646

647
648
649
650
651
652

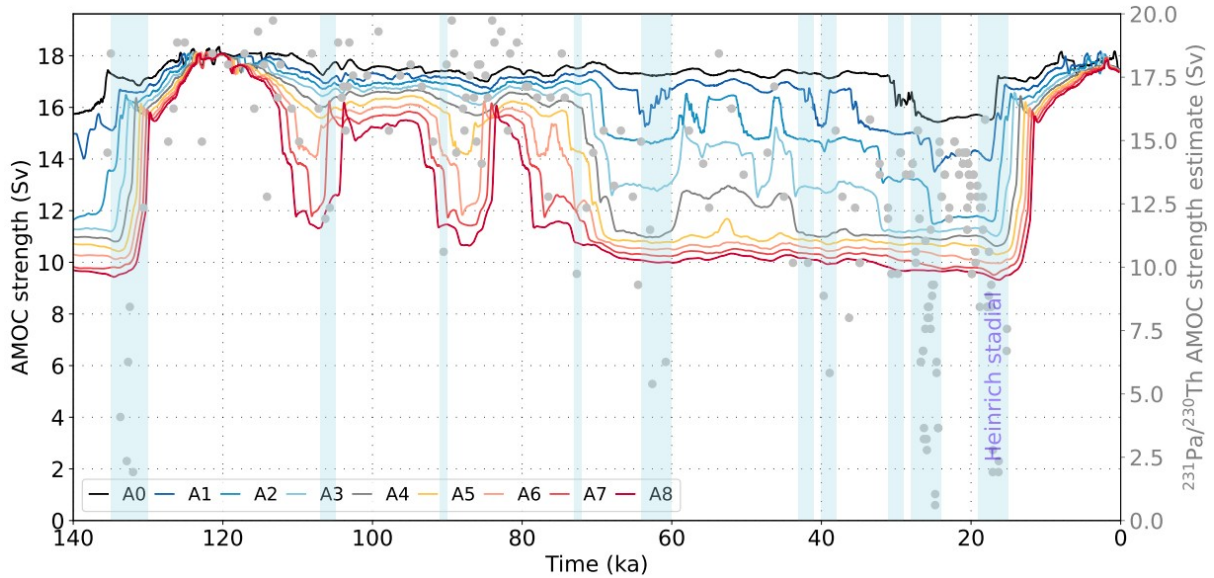


653 Figure 7: Simulated and reconstructed SST differences from PI over the last glacial cycle in
654 the North Atlantic (a, reconstruction by Candy and Alonso-Garcia, 2018) and on the Iberian
655 Margin (b, reconstruction by Davtian and Bard, 2023). The model data was interpolated to
656 the time points for which proxy reconstructions exist.

657

658 Unlike in our simulations, most GCMs participating in PMIP4 do not show a shoaling or
659 weakening of the overturning cell under LGM boundary conditions (Sherriff-Tadano and
660 Klockmann, 2021). The difference could arise from the static wind fields that we prescribed,
661 since an ice-sheet related increase in wind speeds over the North Atlantic leads to a
662 strengthened AMOC (Klockmann et al., 2018), or different representations of processes
663 affecting AABW density changes (e.g. brine rejection, Bouttes et al., 2011). A shallower and
664 likely weaker AMOC during peak glacials is however consistent with observational data
665 (Lynch-Stieglitz et al., 2017, Pöppelmeier et al., 2023). In Fig. 7, simulated SST changes
666 from the Rockall Trough and the Iberian Margin are compared to proxy-based
667 reconstructions. Circulation changes alter the distribution of heat in the North Atlantic, and
668 simulated SST patterns are strongly affected by AMOC changes. In response to the
669 stepwise AMOC weakening, simulated Atlantic SST also transitioned stepwise from
670 interglacials to glacial maxima. Step changes are also an established feature of Atlantic SST
671 reconstructions over the last glacial cycle (Fig. 7), with the biggest steps at 120-110 ka and
672 80-60 ka also captured in our simulations. During glacial inception between 120 ka and 70
673 ka, the amplitudes of reconstructed SST changes in both locations resemble those simulated
674 with strong radiative forcing (simulations A6, A7, A8). Afterwards, SSTs in those simulations
675 decreased more than in the reconstructions, and the latter align more closely with weaker
676 radiative forcing (simulations A3, A4). After ~70 ka, shorter millennial-scale events (Heinrich
677 and Dansgaard-Oeschger), that were not included in our simulations, were more frequent
678 than before and could affect the comparability between reconstructed and simulated SST.

679 Additionally, the further into the glacial cycle, the more the topography and wind fields would
 680 have deviated from their pre-industrial states that we kept constant throughout the
 681 simulations. These factors could have caused a shift in AMOC and SST changes that are
 682 not captured by our simulations.
 683

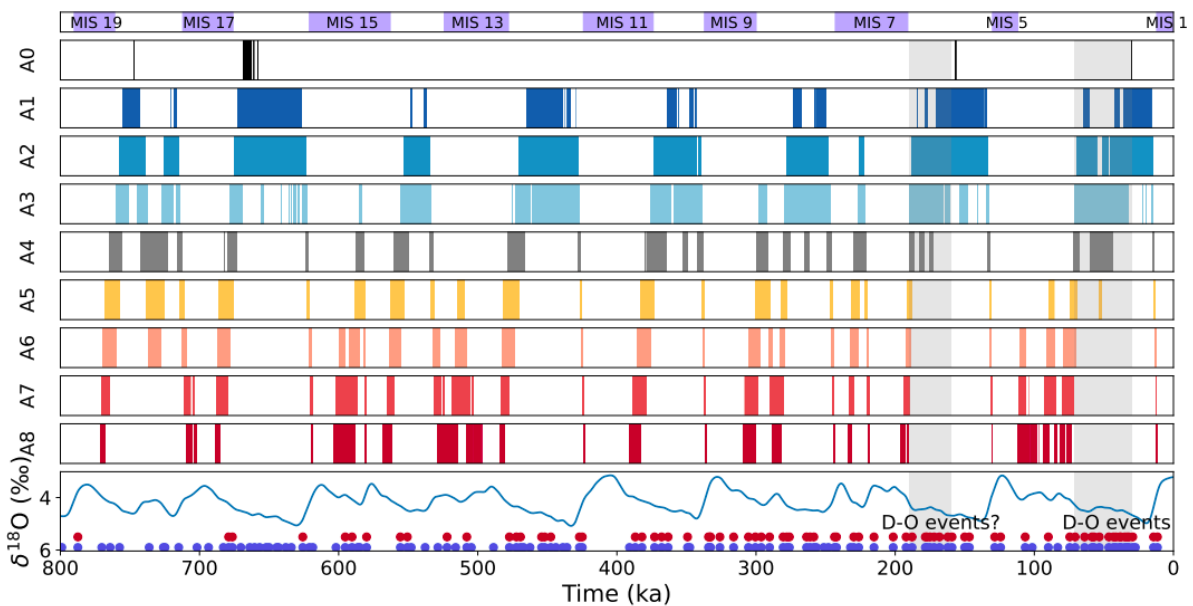


684
 685 Figure 8: Simulated AMOC changes due to thermal forcing over the last 140 kyr. Gray dots
 686 indicate AMOC strength estimated from $^{231}\text{Pa}/^{230}\text{Th}$ (Böhm et al., 2015, Lippold et al., 2009)
 687 by assuming a sensitivity of -0.0024 Sv^{-1} (Rempfer et al., 2017).
 688

689 Fig. 8 compares the simulated changes in AMOC strength over the last 120 kyr in simulation
 690 set A to indications of AMOC weakening based on $^{231}\text{Pa}/^{230}\text{Th}$ from the Bermuda Rise (Böhm
 691 et al., 2015). The simulations A2-A4 have PI-LGM GMST differences of 4.7-6.2°C (within the
 692 proxy-constrained and PMIP range and close to the most recent estimate of 6.1°C by
 693 Tierney et al., 2020) and show a shift to a weaker AMOC at the beginning of MIS 4 around
 694 70 ka ago, when a negative $^{231}\text{Pa}/^{230}\text{Th}$ shift occurred. While the simulated radiation-driven
 695 AMOC changes cannot explain weaker or collapsed circulation modes (<11 Sv) during
 696 Heinrich stadials, this comparison shows that the long term AMOC weakening during glacial
 697 phases could have been driven by temperature changes. It is important to note that AMOC
 698 strength estimates based on this $^{231}\text{Pa}/^{230}\text{Th}$ record need to be treated with caution.
 699 Pöppelmeier et al. (2021; 2023) showed a strong local influence on sedimentary proxies at
 700 this site, and we did not correct the $^{231}\text{Pa}/^{230}\text{Th}$ signal for potential productivity changes.
 701

702 **3.4. Meta-stable AMOC modes over the last 788 kyr**
 703

704 Finally, we can test whether our simulations capture the periods with increased frequency of
 705 AMOC transitions that are indicated by proxies over the last eight glacial cycles. Using our
 706 788 kyr long simulations in simulation set A, we determined how often and when the
 707 radiative forcing pushed the AMOC into ‘excitable’ circulation modes, i.e. modes II and III,
 708 which showed more frequent AMOC strength shifts than the interglacial and glacial modes I
 709 and IV (Fig. 1 and SI.2), and how this varied with the applied forcing strength (Fig. 9). In all
 710 simulations, the AMOC transitioned into such excitable modes in all of the past eight glacial
 711 cycles, but the timing of these shifts varied. For example, during the last glacial cycle, the
 712 simulations A2-A4 exhibited an intermediate circulation mode during MIS 3 (57-29 ka), when
 713 frequent AMOC mode shifts occurred (see Fig. 1). Similar rapid mode switches occurred
 714 earlier in the glacial cycle, i.e. during MIS 5d-e in simulations A6-A8. In these simulations,
 715 the AMOC already transitioned into the persistent glacial circulation mode IV at the
 716 beginning of MIS 4 (71-57 ka), in which North Atlantic density profiles are more stable. In
 717 simulations A1-A3, the AMOC persisted in these modes for several tens of thousands of
 718 years at a time, during most glacials. Under stronger radiative forcing, the periods in which
 719 AMOC adopted these modes were shorter and mostly occurred at the start of glacial cycles.
 720



721
 722 Figure 9: Occurrence of intermediate AMOC modes II and III due to radiative forcing over the
 723 last 788 kyr in simulation set A. The time periods with intermediate AMOC modes are
 724 marked as vertical bars, each row showing the results for a different forcing magnitude from
 725 simulation set A. At the bottom, $\delta^{18}\text{O}$ from Lisiecki and Raymo (2005) is shown for reference,
 726 alongside the time period with confirmed and suspected Dansgaard-Oeschger events (light
 727 gray bars based on Rousseau et al., 2020, blue and red circles are based on reconstructions

728 | Barker et al., 2011, who used two different detection thresholds). The gray bars indicate the
729 | periods in MIS3-4 and MIS6 with confirmed Dansgaard-Oeschger events.

730

731 We can assess the skill of our simulations at predicting 'excitable' AMOC modes from the
732 radiative forcing by comparing the output with records of high AMOC variability in the past.
733 Simulations A3 and A4 shift into a meta-stable circulation mode during MIS 3, and similarly
734 between 190 and 160 ka during the penultimate glacial cycle, and prior to each previous
735 glacial maximum but not during the glacial maxima themselves. An 'excitable' AMOC mode
736 during these intervals seems realistic given the high frequency of Dansgaard-Oeschger
737 events in MIS 3 and the suspected occurrence of Dansgaard-Oeschger events during MIS 6
738 (191-123 ka, Rousseau et al. 2020). Similarly, Barker et al. (2011), who predicted the
739 occurrence of Dansgaard-Oeschger events during previous glacial cycles based on the
740 Antarctic methane and temperature records (with two different identification thresholds, red
741 and blue circles in Fig. 9) following the approach of Siddall et al. (2006), found a high
742 frequency of occurrence of Dansgaard-Oeschger events during MIS 3 and 6, but also
743 throughout most other glacial phases. None of our simulations predicts such a ubiquity of
744 'excitable' AMOC modes, possibly due to the prescribed boundary conditions although the
745 detection method of Barker et al. (2011) is also more uncertain for glacial cycles further back
746 in time. The consistency of the simulated radiation-induced AMOC instability with
747 observational indication of millennial-scale AMOC variability at least during MIS 3 and 6 in
748 simulations A3 and A4 suggests that these could present a more realistic temporal AMOC
749 evolution than the others. Simulations A3 and A4 also exhibit PI-LGM temperature
750 differences of 5.4 and 6.2°C, respectively, close to the proxy-constrained reconstruction
751 (Tierney et al., 2020), and roughly reproduce the reconstructed regional SST changes and
752 reduced circulation strength in MIS 3 and 2 (Fig. 7 and 8).

753

754 Thermal conditioning of AMOC excitability is in line with studies that found the existence of a
755 'sweet spot' in atmospheric CO₂ radiative forcing which is particularly conducive to short,
756 abrupt AMOC perturbations and/or self-sustained AMOC oscillations (e.g. Li and Born, 2019,
757 Vettoretti et al., 2022). Yet, our simulations do not produce such perturbations, partly due to
758 the smoothed forcing and static wind fields (see discussion of model limitations above). The
759 transient circulation mode switches in response to orbitally-paced radiation changes in our
760 simulations are much weaker than those found in other studies (Vettoretti et al., 2022,
761 Klockmann et al., 2018, Kuniyoshi et al., 2022), and our simulations do not contain
762 oscillations that could directly be compared to Dansgaard-Oeschger events.

763

764

765 **4 Conclusions**

766

767 Our study demonstrates the existence of thermal AMOC thresholds and multiple stable
768 circulation modes in the Bern3D model. This adds to previous studies showing that thermal
769 AMOC thresholds emerge in a range of Earth system models varying in complexity and
770 number of components coupled (Zhang et al., 1993), in particular, they also arise in an
771 energetically and hydrologically coupled ocean-sea ice-atmosphere model of intermediate
772 complexity like Bern3D. These thresholds shape the response in the simulated AMOC to
773 radiative orbital and atmospheric composition-driven temperature changes over the last 788
774 kyr. During this period the AMOC transitions between up to four persistent circulation modes.
775 The full glacial and interglacial circulation modes are most frequently simulated, as relatively
776 strong forcing is required to push the AMOC out of them. In contrast, the intermediate AMOC
777 modes are more sensitive to perturbations as small variations in orbital and radiative forcing
778 are able to push the circulation out of these modes. This behaviour resembles the one found
779 in more complex General Circulation Models that exhibit self-sustained oscillations at
780 'sweetspot' CO₂ levels, which lie between glacial and interglacial values. Our simulations
781 suggest that radiative forcing could have created time periods during which highly sensitive
782 intermediate AMOC modes occurred repeatedly over the last 788 kyr.

783

784 **Data availability**

785

786 All simulation output necessary to produce the figures in this manuscript are available at
787 <https://doi.org/10.5281/zenodo.8424878>

788 Proxy data plotted against the simulation output for comparison was taken from public
789 repositories and are available via the citations provided.

790

791 **Author contributions**

792

793 AJT ran the simulations. MA analysed the output and drafted the manuscript. All authors
794 contributed to the interpretation of the results and the final manuscript text.

795

796 **Conflicts of interest**

797

798 The authors declare that they have no conflict of interest.

799

800 **Acknowledgements**

801

802 MA, AJT and FJ were financially supported by the Swiss National Science Foundation
803 (#200020_200511).

804

805 FP was financially supported by the European Union's Horizon 2020 research and
806 innovation programme under grant agreements no. 101023443 (project CliMoTran).

807

808 TFS and FP were financially supported by the European Union's Horizon 2020 research and
809 innovation programme under grant agreements no. 820970 (project TiPES), and the Swiss
810 National Science Foundation's project 200020_200492.

811

812 Calculations were performed on UBELIX (<http://www.id.unibe.ch/hpc>), the HPC cluster at the
813 University of Bern.

814

815

816

817 **References**

818

819 **Aeberhardt, M., Blatter, M. and Stocker, T.F., 2000. Variability on the century time**
820 **scale and regime changes in a stochastically forced zonally averaged ocean-**
821 **atmosphere model. *Geophysical Research Letters*, 27(9), pp.1303-1306.**

822

823 Albani, S., Balkanski, Y., Mahowald, N., Winckler, G., Maggi, V. and Delmonte, B., 2018. Aerosol-
824 climate interactions during the Last Glacial Maximum. *Current Climate Change Reports*, 4, pp.99-114.

825

826 Ando, T. and Oka, A., 2021. Hysteresis of the glacial Atlantic meridional overturning
827 circulation controlled by thermal feedbacks. *Geophysical Research Letters*, 48(24),
828 p.e2021GL095809.

829

830 Armstrong, E., Izumi, K. and Valdes, P., 2022. Identifying the mechanisms of DO-scale oscillations in
831 a GCM: a salt oscillator triggered by the Laurentide ice sheet. *Climate Dynamics*, pp.1-19.

832

833 Arzel, O., England, M.H. and Sijp, W.P., 2008. Reduced stability of the Atlantic meridional overturning
834 circulation due to wind stress feedback during glacial times. *Journal of climate*, 21(23), pp.6260-6282.

835

836 Banderas, R., Álvarez-Solas, J. and Montoya, M., 2012. Role of CO₂ and Southern Ocean winds in
837 glacial abrupt climate change. *Climate of the Past*, 8(3), pp.1011-1021.

838

839 Bard, E., Arnold, M., Maurice, P., Duprat, J., Moyes, J. and Duplessy, J.C., 1987. Retreat velocity of
840 the North Atlantic polar front during the last deglaciation determined by ^{14}C accelerator mass
841 spectrometry. *Nature*, 328(6133), pp.791-794.
842

843 Barker, S., Knorr, G., Edwards, R.L., Parrenin, F., Putnam, A.E., Skinner, L.C., Wolff, E. and Ziegler,
844 M., 2011. 800,000 years of abrupt climate variability. *science*, 334(6054), pp.347-351.
845

846 Barker, S., Chen, J., Gong, X., Jonkers, L., Knorr, G. and Thornalley, D., 2015. Icebergs not the
847 trigger for North Atlantic cold events. *Nature*, 520(7547), pp.333-336.
848

849 Bereiter, B., Eggleston, S., Schmitt, J., Nehrbass-Ahles, C., Stocker, T.F., Fischer, H., Kipfstuhl, S.
850 and Chappellaz, J., 2015. Revision of the EPICA Dome C CO_2 record from 800 to 600 kyr before
851 present. *Geophysical Research Letters*, 42(2), pp.542-549.
852

853 Berger, A., 1978. Long-term variations of caloric insolation resulting from the Earth's orbital elements.
854 *Quaternary research*, 9(2), pp.139-167.
855

856 Berger, A. and Loutre, M.F., 1991. Insolation values for the climate of the last 10 million years.
857 *Quaternary science reviews*, 10(4), pp.297-317.
858

859 Berger, V.W. and Zhou, Y., 2014. Kolmogorov–smirnov test: Overview. Wiley statsref: Statistics
860 reference online.
861

862 Böhm, E., Lippold, J., Gutjahr, M., Frank, M., Blaser, P., Antz, B., Fohlmeister, J., Frank, N.,
863 Andersen, M.B. and Deininger, M., 2015. Strong and deep Atlantic meridional overturning circulation
864 during the last glacial cycle. *Nature*, 517(7532), pp.73-76.
865

866 Bouttes, N., Paillard, D., Roche, D.M., Brovkin, V. and Bopp, L., 2011. Last Glacial Maximum CO_2
867 and $\delta^{13}\text{C}$ successfully reconciled. *Geophysical Research Letters*, 38(2).
868

869 Bozbiyik, A., Steinacher, M., Joos, F., Stocker, T.F. and Menviel, L., 2011. Fingerprints of changes in
870 the terrestrial carbon cycle in response to large reorganizations in ocean circulation. *Climate of the*
871 *Past*, 7(1), pp.319-338.
872

873 Broecker, W.S., Blanton, S., Smethie Jr, W.M. and Ostlund, G., 1991. Radiocarbon decay and oxygen
874 utilization in the deep Atlantic Ocean. *Global Biogeochemical Cycles*, 5(1), pp.87-117.
875

876 Broecker, W.S., 1994. Massive iceberg discharges as triggers for global climate change. *Nature*,
877 372(6505), pp.421-424.
878

879 Brown, N. and Galbraith, E.D., 2016. Hosed vs. unhosed: interruptions of the Atlantic Meridional
880 Overturning Circulation in a global coupled model, with and without freshwater forcing. *Climate of the*
881 *Past*, 12(8), pp.1663-1679.
882

883 Buizert, C. and Schmittner, A., 2015. Southern Ocean control of glacial AMOC stability and
884 Dansgaard-Oeschger interstadial duration. *Paleoceanography*, 30(12), pp.1595-1612.
885

886 Candy, I. and Alonso-Garcia, M., 2018. A 1 Ma sea surface temperature record from the North
887 Atlantic and its implications for the early human occupation of Britain. *Quaternary Research*, 90(2),
888 pp.406-417.
889

890 Dansgaard, W., Johnsen, S.J., Clausen, H.B., Dahl-Jensen, D., Gundestrup, N.S., Hammer, C.U.,
891 Hvidberg, C.S., Steffensen, J.P., Sveinbjörnsdóttir, A.E., Jouzel, J. and Bond, G., 1993. Evidence for
892 general instability of past climate from a 250-kyr ice-core record. *nature*, 364(6434), pp.218-220.
893

894 Davtian, N. and Bard, E., 2023. A new view on abrupt climate changes and the bipolar seesaw based
895 on paleotemperatures from Iberian Margin sediments. *Proceedings of the National Academy of*
896 *Sciences*, 120(12), p.e2209558120.
897

898 De Boer, A.M., Gnanadesikan, A., Edwards, N.R. and Watson, A.J., 2010. Meridional density
899 gradients do not control the Atlantic overturning circulation. *Journal of Physical Oceanography*, 40(2),
900 pp.368-380.
901

902 de Vries, P. and Weber, S.L., 2005. The Atlantic freshwater budget as a diagnostic for the existence
903 of a stable shut down of the meridional overturning circulation. *Geophysical Research Letters*, 32(9).
904

905 Edwards, N. R., Willmott, A. J., and Killworth, P. D.: On the role of topography and wind stress on the
906 stability of the thermohaline circulation, *J. Phys. Oceanogr.*, 28, 756–778,
907 [https://doi.org/10.1175/1520-0485\(1998\)028<0756:OTROTA>2.0.CO;2](https://doi.org/10.1175/1520-0485(1998)028<0756:OTROTA>2.0.CO;2), 1998.
908

909 Fischer, H., Meissner, K.J., Mix, A.C., Abram, N.J., Austermann, J., Brovkin, V., Capron, E.,
910 Colombaroli, D., Daniaux, A.L., Dyez, K.A. and Felis, T., 2018. Palaeoclimate constraints on the impact
911 of 2 C anthropogenic warming and beyond. *Nature geoscience*, 11(7), pp.474-485.
912

913 Galbraith, E. and de Lavergne, C., 2019. Response of a comprehensive climate model to a broad
914 range of external forcings: relevance for deep ocean ventilation and the development of late Cenozoic
915 ice ages. *Climate Dynamics*, 52, pp.653-679.
916

917 Ganopolski, A. and Rahmstorf, S., 2001. Rapid changes of glacial climate simulated in a coupled
918 climate model. *Nature*, 409(6817), pp.153-158.

919

920 Gregory, J.M., Dixon, K.W., Stouffer, R.J., Weaver, A.J., Driesschaert, E., Eby, M., Fichfet, T.,
921 Hasumi, H., Hu, A., Jungclaus, J.H. and Kamenkovich, I.V., 2005. A model intercomparison of
922 changes in the Atlantic thermohaline circulation in response to increasing atmospheric CO₂
923 concentration. *Geophysical Research Letters*, 32(12).

924

925 Griffies, S. M.: The Gent–McWilliams Skew Flux, *J. Phys. Oceanogr.*, 28, 831–841,
926 [https://doi.org/10.1175/1520-0485\(1998\)028<0831:TGMSF>2.0.CO;2](https://doi.org/10.1175/1520-0485(1998)028<0831:TGMSF>2.0.CO;2), 1998.

927

928 Grousset, F.E., Pujol, C., Labeyrie, L., Auffret, G. and Boelaert, A., 2000. Were the North Atlantic
929 Heinrich events triggered by the behavior of the European ice sheets?. *Geology*, 28(2), pp.123-126.

930

931 Haskins, R.K., Oliver, K.I., Jackson, L.C., Wood, R.A. and Drijfhout, S.S., 2020. Temperature
932 domination of AMOC weakening due to freshwater hosing in two GCMs. *Climate Dynamics*, 54,
933 pp.273-286.

934

935 Heinrich, H., 1988. Origin and consequences of cyclic ice rafting in the northeast Atlantic Ocean
936 during the past 130,000 years. *Quaternary research*, 29(2), pp.142-152.

937

938 Hu, A., Meehl, G.A., Han, W., Timmermann, A., Otto-Bliesner, B., Liu, Z., Washington, W.M., Large,
939 W., Abe-Ouchi, A., Kimoto, M. and Lambeck, K., 2012. Role of the Bering Strait on the hysteresis of
940 the ocean conveyor belt circulation and glacial climate stability. *Proceedings of the National Academy*
941 *of Sciences*, 109(17), pp.6417-6422.

942

943 Ivanovic, R.F., Valdes, P.J., Gregoire, L., Flecker, R. and Gutjahr, M., 2014. Sensitivity of modern
944 climate to the presence, strength and salinity of Mediterranean-Atlantic exchange in a global general
945 circulation model. *Climate dynamics*, 42, pp.859-877.

946

947 Jackson, L.C., Schaller, N., Smith, R.S., Palmer, M.D. and Vellinga, M., 2014. Response of the
948 Atlantic meridional overturning circulation to a reversal of greenhouse gas increases. *Climate*
949 *dynamics*, 42, pp.3323-3336.

950

951 Jackson, L.C. and Wood, R.A., 2018. Hysteresis and resilience of the AMOC in an eddy-permitting
952 GCM. *Geophysical Research Letters*, 45(16), pp.8547-8556.

953

954 Jackson, L.C., Alastrué de Asenjo, E., Bellomo, K., Danabasoglu, G., Haak, H., Hu, A., Jungclaus,
955 J.H., Lee, W., Meccia, V.L., Saenko, O. and Shao, A., 2023. Understanding AMOC stability: the North
956 Atlantic hosing model intercomparison project. *Geoscientific Model Development*, 16, pp.1975-1995.

957

958 Johnson, H.L., Cessi, P., Marshall, D.P., Schloesser, F. and Spall, M.A., 2019. Recent contributions of
959 theory to our understanding of the Atlantic meridional overturning circulation. *Journal of Geophysical*
960 *Research: Oceans*, 124(8), pp.5376-5399.

961

962 Joos, F. and Spahni, R., 2008. Rates of change in natural and anthropogenic radiative forcing over
963 the past 20,000 years. *Proceedings of the National Academy of Sciences*, 105(5), pp.1425-1430.

964

965 Joos, H., Madonna, E., Witlox, K., Ferrachat, S., Wernli, H. and Lohmann, U., 2017. Effect of
966 anthropogenic aerosol emissions on precipitation in warm conveyor belts in the western North Pacific
967 in winter—a model study with ECHAM6-HAM. *Atmospheric chemistry and physics*, 17(10), pp.6243-
968 6255.

969

970 Kageyama, M., Harrison, S.P., Kapsch, M.L., Lofverstrom, M., Lora, J.M., Mikolajewicz, U., Sherriff-
971 Tadano, S., Vadsaria, T., Abe-Ouchi, A., Bouttes, N. and Chandan, D., 2021. The PMIP4 Last Glacial
972 Maximum experiments: preliminary results and comparison with the PMIP3 simulations. *Climate of the*
973 *Past*, 17(3), pp.1065-1089.

974

975 Klockmann, M., Mikolajewicz, U. and Marotzke, J., 2018. Two AMOC states in response to
976 decreasing greenhouse gas concentrations in the coupled climate model MPI-ESM. *Journal of*
977 *Climate*, 31(19), pp.7969-7984.

978

979 Klockmann, M., Mikolajewicz, U., Kleppin, H. and Marotzke, J., 2020. Coupling of the subpolar gyre
980 and the overturning circulation during abrupt glacial climate transitions. *Geophysical Research*
981 *Letters*, 47(21), p.e2020GL090361.

982

983 Knorr, G. and Lohmann, G., 2007. Rapid transitions in the Atlantic thermohaline circulation triggered
984 by global warming and meltwater during the last deglaciation. *Geochemistry, Geophysics,*
985 *Geosystems*, 8(12).

986

987 Knutti, R. and Stocker, T.F., 2002. Limited predictability of the future thermohaline circulation close to
988 an instability threshold. *Journal of Climate*, 15(2), pp.179-186.

989

990 Kuniyoshi, Y., Abe-Ouchi, A., Sherriff-Tadano, S., Chan, W.L. and Saito, F., 2022. Effect of Climatic
991 Precession on Dansgaard-Oeschger-Like Oscillations. *Geophysical Research Letters*, 49(6),
992 p.e2021GL095695.

993

994 Li, C. and Born, A., 2019. Coupled atmosphere-ice-ocean dynamics in Dansgaard-Oeschger events.
995 *Quaternary Science Reviews*, 203, pp.1-20.

996

997 Lippold, J., Grützner, J., Winter, D., Lahaye, Y., Mangini, A. and Christl, M., 2009. Does sedimentary
998 $^{231}\text{Pa}/^{230}\text{Th}$ from the Bermuda Rise monitor past Atlantic meridional overturning circulation?.
999 *Geophysical Research Letters*, 36(12).

1000

1001 Lisiecki, L. E. & Raymo, M. E. A, 2005. Pliocene-Pleistocene stack of 57 globally distributed benthic
1002 $\delta^{18}\text{O}$ records. *Paleoceanography* 20, PA1003, doi:10.1029/2004PA001071.

1003

1004 Lisiecki, L.E. and Stern, J.V., 2016. Regional and global benthic $\delta^{18}\text{O}$ stacks for the last glacial cycle.
1005 *Paleoceanography*, 31(10), pp.1368-1394.

1006

1007 Liu, W., Xie, S.P., Liu, Z. and Zhu, J., 2017. Overlooked possibility of a collapsed Atlantic Meridional
1008 Overturning Circulation in warming climate. *Science Advances*, 3(1), p.e1601666.

1009

1010 Lohmann, J., Dijkstra, H.A., Jochum, M., Lucarini, V. and Ditlevsen, P.D., 2023. Multistability and
1011 Intermediate Tipping of the Atlantic Ocean Circulation. arXiv preprint arXiv:2304.05664.

1012

1013 Loulergue, L., Schilt, A., Spahni, R., Masson-Delmotte, V., Blunier, T., Lemieux, B., Barnola, J.M.,
1014 Raynaud, D., Stocker, T.F. and Chappellaz, J., 2008. Orbital and millennial-scale features of
1015 atmospheric CH_4 over the past 800,000 years. *Nature*, 453(7193), pp.383-386.

1016

1017 Lynch-Stieglitz, J., 2017. The Atlantic meridional overturning circulation and abrupt climate change.
1018 *Annual review of marine science*, 9, pp.83-104.

1019

1020 Malmierca-Vallet, Irene, Louise C. Sime and the D-O community members. "Dansgaard-Oeschger
1021 events in climate models: Review and baseline MIS3 protocol." *Climate of the Past*, 19(5), pp.915-
1022 942.

1023

1024 Manabe, S. and Stouffer, R.J., 1993. Century-scale effects of increased atmospheric CO_2 on the
1025 ocean-atmosphere system. *Nature*, 364(6434), pp.215-218.

1026

1027 Masson-Delmotte, V., Schulz, M., Abe-Ouchi, A., Beer, J., Ganopolski, A., González Rouco, J.F.,
1028 Jansen, E., Lambeck, K., Luterbacher, J., Naish, T. and Osborn, T., 2013. Information from
1029 paleoclimate archives. In IPCC AR5 Climate Change 2013 - The Physical Science Basis (eds
1030 Stocker, T. et al.), 383464, p.2013.

1031

1032 Menary, M.B., Roberts, C.D., Palmer, M.D., Halloran, P.R., Jackson, L., Wood, R.A., Müller, W.A.,
1033 Matei, D. and Lee, S.K., 2013. Mechanisms of aerosol-forced AMOC variability in a state of the art
1034 climate model. *Journal of Geophysical Research: Oceans*, 118(4), pp.2087-2096.

1035

1036 Menviel, L., Timmermann, A., Mouchet, A. and Timm, O., 2008. Meridional reorganizations of marine
1037 and terrestrial productivity during Heinrich events. *Paleoceanography*, 23(1).
1038

1039 Menviel, L., Joos, F. and Ritz, S.P., 2012. Simulating atmospheric CO₂, ¹³C and the marine carbon
1040 cycle during the Last Glacial–Interglacial cycle: possible role for a deepening of the mean
1041 remineralization depth and an increase in the oceanic nutrient inventory. *Quaternary Science*
1042 *Reviews*, 56, pp.46-68.
1043

1044 Mikolajewicz, U., Santer, B.D. and Maier-Reimer, E., 1990. Ocean response to greenhouse warming.
1045 *Nature*, 345(6276), pp.589-593.
1046

1047 Müller, S.A., Joos, F., Edwards, N.R. and Stocker, T.F., 2006. Water mass distribution and ventilation
1048 time scales in a cost-efficient, three-dimensional ocean model. *Journal of Climate*, 19(21), pp.5479-
1049 5499.
1050

1051 Oeschger, H., Beer, J., Siegenthaler, U., Stauffer, B., Dansgaard, W. and Langway, C.C., 1984. Late
1052 glacial climate history from ice cores. *Climate processes and climate sensitivity*, 29, pp.299-306.
1053

1054 Oka, A., Hasumi, H. and Abe-Ouchi, A., 2012. The thermal threshold of the Atlantic meridional
1055 overturning circulation and its control by wind stress forcing during glacial climate. *Geophysical*
1056 *Research Letters*, 39(9).
1057

1058 Oka, A., Abe-Ouchi, A., Sherriff-Tadano, S., Yokoyama, Y., Kawamura, K. and Hasumi, H., 2021.
1059 Glacial mode shift of the Atlantic meridional overturning circulation by warming over the Southern
1060 Ocean. *Communications Earth & Environment*, 2(1), p.169.
1061

1062 Okazaki, Y., Timmermann, A., Menviel, L., Harada, N., Abe-Ouchi, A., Chikamoto, M.O., Mouchet, A.
1063 and Asahi, H., 2010. Deepwater formation in the North Pacific during the last glacial termination.
1064 *Science*, 329(5988), pp.200-204.
1065

1066 Pedro, J.B., Jochum, M., Buizert, C., He, F., Barker, S. and Rasmussen, S.O., 2018. Beyond the
1067 bipolar seesaw: Toward a process understanding of interhemispheric coupling. *Quaternary Science*
1068 *Reviews*, 192, pp.27-46.
1069

1070 Pöppelmeier, F., Scheen, J., Jeltsch-Thömmes, A. and Stocker, T.F., 2020. Simulated stability of the
1071 AMOC during the Last Glacial Maximum under realistic boundary conditions. *Climate of the Past*,
1072 2021 17, no. 2 (2021): 615-632.
1073

1074 Pöppelmeier, F., Scheen, J., Jeltsch-Thömmes, A. and Stocker, T.F., 2021. Simulated stability of the
1075 Atlantic meridional overturning circulation during the Last Glacial Maximum. *Climate of the Past*,
1076 17(2), pp.615-632.

1077

1078 Pöppelmeier, F., Jeltsch-Thömmes, A., Lippold, J., Joos, F. and Stocker, T.F., 2023. Multi-proxy
1079 constraints on Atlantic circulation dynamics since the last ice age. *Nature geoscience*, 16(4), pp.349-
1080 356.

1081

1082 Praetorius, S.K. and Mix, A.C., 2014. Synchronization of North Pacific and Greenland climates
1083 preceded abrupt deglacial warming. *Science*, 345(6195), pp.444-448.

1084

1085 Rahmstorf, S., 1996. On the freshwater forcing and transport of the Atlantic thermohaline circulation,
1086 *Clim. Dyn.*, 12, 799–811.

1087

1088 Rahmstorf, S., 1998. Influence of Mediterranean outflow on climate. *Eos, Transactions American*
1089 *Geophysical Union*, 79(24), pp.281-282.

1090

1091 Rempfer, J., Stocker, T.F., Joos, F., Lippold, J. and Jaccard, S.L., 2017. New insights into cycling of
1092 231Pa and 230Th in the Atlantic Ocean. *Earth and Planetary Science Letters*, 468, pp.27-37.

1093

1094 Ritz, S.P., Stocker, T.F. and Joos, F., 2011. A coupled dynamical ocean–energy balance atmosphere
1095 model for paleoclimate studies. *Journal of Climate*, 24(2), pp.349-375.

1096

1097 Roth, R., Ritz, S. P., and Joos, F., 2014: Burial-nutrient feedbacks amplify the sensitivity of
1098 atmospheric carbon dioxide to changes in organic matter remineralisation, *Earth Syst. Dynam.*, 5,
1099 321–343.

1100

1101 Rousseau, D.D., Antoine, P., Boers, N., Lacroix, F., Ghil, M., Lomax, J., Fuchs, M., Debret, M., Hatté,
1102 C., Moine, O. and Gauthier, C., 2020. Dansgaard–Oeschger-like events of the penultimate climate
1103 cycle: the loess point of view. *Climate of the Past*, 16(2), pp.713-727.

1104

1105 Ruddiman, W.F. and McIntyre, A., 1981. The North Atlantic Ocean during the last deglaciation.
1106 *Palaeogeography, Palaeoclimatology, Palaeoecology*, 35, pp.145-214.

1107

1108 Severinghaus, J.P., Beaudette, R., Headly, M.A., Taylor, K. and Brook, E.J., 2009. Oxygen-18 of O2
1109 records the impact of abrupt climate change on the terrestrial biosphere. *Science*, 324(5933),
1110 pp.1431-1434.

1111

1112 Sherriff-Tadano, S. and Klockmann, M., 2021. PmiP contributions to understanding the deep ocean
1113 circulation of the last glacial maximum. *Past Global Changes Magazine*, 29(2), pp.84-85.

1114
1115 Sherriff-Tadano, S., Abe-Ouchi, A., Yoshimori, M., Ohgaito, R., Vadsaria, T., Chan, W.L., Hotta, H.,
1116 Kikuchi, M., Kodama, T., Oka, A. and Suzuki, K., 2023. Southern Ocean surface temperatures and
1117 cloud biases in climate models connected to the representation of glacial deep ocean circulation.
1118 *Journal of Climate*, 36(11), pp.3849-3866.
1119
1120 Siddall, M., T.F. Stocker, T. Blunier, R. Spahni, J. McManus, and E. Bard, Using a maximum simplicity
1121 paleoclimate model to simulate millennial variability during the last four glacial periods, *Quat. Sci.*
1122 *Rev.*, 25, 3185-3197, 2006.
1123
1124 Stocker, T.F., and D.G. Wright, Rapid transitions of the ocean's deep circulation induced by changes
1125 in surface water fluxes, *Nature*, 351, 729-732, 1991.
1126
1127 Stocker, T.F. and Schmittner, A., 1997. Influence of CO₂ emission rates on the stability of the
1128 thermohaline circulation. *Nature*, 388(6645), pp.862-865.
1129
1130 Stocker, T.F., 2000. Past and future reorganizations in the climate system. *Quaternary Science*
1131 *Reviews*, 19(1-5), pp.301-319.
1132
1133 Stocker, T.F. and Johnsen, S.J., 2003. A minimum thermodynamic model for the bipolar seesaw.
1134 *Paleoceanography*, 18(4).
1135
1136 Stommel, H., 1961. Thermohaline convection with two stable regimes of flow. *Tellus*, 13(2), 224– 230.
1137 <https://doi.org/10.3402/tellusb.v13i2.12985>
1138
1139 Swingedouw, D., Colin, C., Eynaud, F., Ayache, M. and Zaragosi, S., 2019. Impact of freshwater
1140 release in the Mediterranean Sea on the North Atlantic climate. *Climate Dynamics*, 53, pp.3893-3915.
1141
1142 Swingedouw, D., Houssais, M.N., Herbaut, C., Blaizot, A.C., Devilliers, M. and Deshayes, J., 2022.
1143 AMOC Recent and Future Trends: A Crucial Role for Oceanic Resonance and Greenland Melting?.
1144 *Frontiers in Climate*, p.32.
1145
1146 Tetard, M., Licari, L. and Beaufort, L., 2017. Oxygen history off Baja California over the last 80 kyr: A
1147 new foraminiferal-based record. *Paleoceanography*, 32(3), pp.246-264.
1148
1149 Tierney, J.E., Zhu, J., King, J., Malevich, S.B., Hakim, G.J. and Poulsen, C.J., 2020. Glacial cooling
1150 and climate sensitivity revisited. *Nature*, 584(7822), pp.569-573.
1151
1152 Timmermann, A. and Friedrich, T., 2016. Late Pleistocene climate drivers of early human migration.
1153 *Nature*, 538(7623), pp.92-95.

1154
1155 Vettoretti, G., Ditlevsen, P., Jochum, M. and Rasmussen, S.O., 2022. Atmospheric CO2 control of
1156 spontaneous millennial-scale ice age climate oscillations. *Nature Geoscience*, 15(4), pp.300-306.
1157
1158 Wang, Y.J., Cheng, H., Edwards, R.L., An, Z.S., Wu, J.Y., Shen, C.C. and Dorale, J.A., 2001. A high-
1159 resolution absolute-dated late Pleistocene monsoon record from Hulu Cave, China. *Science*,
1160 294(5550), pp.2345-2348.
1161
1162 Weijer, W., Cheng, W., Drijfhout, S.S., Fedorov, A.V., Hu, A., Jackson, L.C., Liu, W., McDonagh, E.L.,
1163 Mecking, J.V. and Zhang, J., 2019. Stability of the Atlantic Meridional Overturning Circulation: A
1164 review and synthesis. *Journal of Geophysical Research: Oceans*, 124(8), pp.5336-5375.
1165
1166 Weijer, W., Cheng, W., Garuba, O.A., Hu, A. and Nadiga, B.T., 2020. CMIP6 models predict
1167 significant 21st century decline of the Atlantic meridional overturning circulation. *Geophysical*
1168 *Research Letters*, 47(12), p.e2019GL086075.
1169
1170 Winckler, G., Anderson, R.F., Fleisher, M.Q., McGee, D. and Mahowald, N., 2008. Covariant glacial-
1171 interglacial dust fluxes in the equatorial Pacific and Antarctica. *science*, 320(5872), pp.93-96.
1172
1173 Yang, H., Wang, K., Dai, H., Wang, Y. and Li, Q., 2016. Wind effect on the Atlantic meridional
1174 overturning circulation via sea ice and vertical diffusion. *Climate Dynamics*, 46, pp.3387-3403.
1175
1176 Zhang, S., Greatbatch, R.J. and Lin, C.A., 1993. A reexamination of the polar halocline catastrophe
1177 and implications for coupled ocean-atmosphere modeling. *Journal of Physical Oceanography*, 23(2),
1178 pp.287-299.
1179 |
1180 [Zhang, X., Lohmann, G., Knorr, G. and Xu, X., 2013. Different ocean states and transient](#)
1181 [characteristics in Last Glacial Maximum simulations and implications for deglaciation. *Climate of the*](#)
1182 [Past, 9\(5\), pp.2319-2333.](#)
1183 |
1184 Zhang, X., Prange, M., Merkel, U. and Schulz, M., 2014. Instability of the Atlantic overturning
1185 circulation during Marine Isotope Stage 3. *Geophysical Research Letters*, 41(12), pp.4285-4293.
1186 |
1187 [Zhang, X., Lohmann, G., Knorr, G. and Purcell, C., 2014 \(b\). Abrupt glacial climate shifts controlled by](#)
1188 [ice sheet changes. *Nature*, 512\(7514\), pp.290-294.](#)
1189 |
1190 Zhang, X., Knorr, G., Lohmann, G. and Barker, S., 2017. Abrupt North Atlantic circulation changes in
1191 response to gradual CO2 forcing in a glacial climate state. *Nature Geoscience*, 10(7), pp.518-523.
1192